Mon. Not. R. Astron. Soc. **000**, 1–18 (2010) Printed 25 June 2010 (MN LaTeX style file v2.2)

Spectral imaging of the Sagittarius B2 region in multiple 7-mm molecular lines

P. A. Jones[1,2], ⋆ M. G. Burton[1], N. F. H. Tothill[1,3] and M. R. Cunningham[1,2]
[1]*School of Physics, University of New South Wales, Sydney, NSW 2052, Australia*
[2]*Departamento de Astronomía, Universidad de Chile, Casilla 36-D, Santiago, Chile*
[3]*School of Physics, University of Exeter, Stocker Road, Exeter, EX 4 4 QL, UK*

Accepted . Received ; in original form 2010 April 1

ABSTRACT

We have undertaken a spectral-line imaging survey of a 6×6 arcmin^2 area around Sgr B2 near the centre of the Galaxy, in the range from 30 to 50 GHz, using the Mopra telescope. The spatial resolution varies from 1.0 to 1.4 arcmin and the spectral resolution from 1.6 to 2.7 km s^1 over the frequency range. We present velocity-integrated emission images for 47 lines: 38 molecular lines and 9 radio recombination lines.

There are significant differences between the distributions of different molecules, in part due to spatial differences in chemical abundance across the complex. For example, HNCO and $HOCO^+$ are found preferentially in the north cloud, and CH_2NH near Sgr B2 (N). Some of the differences between lines are due to excitation differences, as shown by the 36.17 and 44.07 GHz lines of CH_3OH, which have maser emission, compared to the 48.37 GHz line of CH_3OH. Other major differences in integrated molecular line distribution are due to absorption of the 7-mm free-free continuum emission (spatially traced by the radio recombination line emission) by intervening molecular material, causing a central dip in the molecular line distributions.

These line distribution similarities and differences have been statistically described by principal component analysis (PCA), and interpreted in terms of simple Sgr B2 physical components of the cooler, lower density envelope, and dense, hot cores Sgr B2 (N), (M) and (S).

Key words: ISM:individual (Sagittarius B2) – ISM:molecules – radio lines:ISM – ISM:kinematics and dynamics.

1 INTRODUCTION

Sagittarius B2 (Sgr B2) is a giant molecular cloud complex near the centre of the Galaxy. There is spectacular star-formation activity, much of it deeply embedded in molecular cores, as traced by the high far-infrared luminosity, compact and ultracompact H II regions (Gaume et al. 1995), with maser emission from water (McGrath, Goss & De Pree 2004), hydroxyl (Gaume & Claussen 1990), formaldehyde (Mehringer et al. 1994) and methanol, both class I and class II (Caswell 1996; Mehringer & Menten 1997).

Three major star-forming centres are located in a north-south line, labelled north, middle and south, Sgr B2 (N), (M) and (S), which have strong continuum radio H II region free-free emission, and submillimetre and millimetre wavelength thermal dust emission (Gordon et al. 1993; Pierce-Price et al. 2000). These cores are surrounded by a larger, less dense envelope.

The hot cores Sgr B2 (N) and (M) are particularly rich in molecules, and so have been the targets of many millimetre spectral-line surveys (Cummins et al. 1986; Turner 1989; Nummelin et al. 1998, 2000; Belloche et al. 2005, 2007). The PRIMOS survey with the Greenbank Telescope (GBT) will survey Sgr B2 (N) over the whole band from 300 MHz to 50 GHz (Remijan et al. 2008).

Sgr B2 is one of the most prominent features of the Central Molecular Zone (CMZ), the bar-shaped (Sawada et al. 2004) molecular region in the central few hundred pc of the Galaxy, as shown in emission of ^{12}CO, ^{12}CO (Oka et al. 1998), CS (Tsuboi, Handa & Ukita 1999) and HNCO (Dahmen et al. 1997), for example.

The distance to Sgr B2 has been measured as $7.8^{+0.8}_{-0.7}$ kpc by Reid et al. (2009), with the proper motion suggesting that Sgr B2 is nearer by 0.13 kpc than the Galactic centre, and the projected distance from the Galactic cen-

⋆ E-mail:pjones@phys.unsw.edu.au

© 2010 RAS

tre is 0.09 kpc. For calculations, we assume the distance to Sgr B2 of 8.0 kpc.

The Sgr B2 molecular cloud has complex kinematics, with the densest core centred on Sgr B2 (M) at velocity 60 - 65 km s^{-1}, and this area corresponding to a 'hole' in the emission in CO and CS at 40 - 50 km s^{-1} (Sato et al. 2000). This has been interpreted by Hasegawa et al. (1994, 2008) as a cloud-cloud collision between a clump at 70 - 80 km s^{-1}, and the 40 - 50 km s^{-1} cloud triggering the current star formation: the collision changes the velocity of material, leaving a deficit (the hole) in the 40 - 50 km s^{-1} range, as material shifts to the intermediate velocity of the 60 - 65 km s^{-1} range.

The spatial distribution in the Sgr B2 molecular cloud is also complex, but can be largely described by a ridge of emission in a north-south line near the Sgr B2 (N), (M) and (S) hot cores, or centred to the west of these cores (Jones et al. 2008a). This ridge continues to a peak 1 arcmin north of Sgr B2 (N), the 'north cloud' which is enhanced in HNCO and $HOCO^+$ (Minh et al. 1998), possibly associated with the shock of the cloud-cloud collision. This ridge of emission coincides with the Sgr B2 extended envelope, as traced by sub-mm dust emission (Pierce-Price et al. 2000).

In this paper, we present results of imaging the Sgr B2 region (6 × 6 arcmin) in multiple spectral lines, over 30 to 50 GHz (the 7-mm band), using the Mopra telescope. This follows on a similar spectral-line imaging survey of Sgr B2 in the 3-mm band, presented as Jones et al. (2008a), Jones, Burton, & Cunningham (2008b) and Jones, Burton, & Lowe (2008c).

2 OBSERVATIONS AND DATA REDUCTION

The observations were made with the 22-m Mopra radio telescope, of the Australia Telescope National Facility (ATNF) using the UNSW-MOPS digital filterbank. The Mopra MMIC receiver has a bandwidth of 8 GHz, and the MOPS backend can cover the full 8-GHz range simultaneously in the broad band mode. This gives four 2.2-GHz sub-bands each with 8192 channels of 0.27 MHz. There is also a zoom mode with up to sixteen spectra (up to four in each 2.2-GHz sub-band) of width 137 MHz. This provides higher spectral resolution with 4096 channels of 0.033 MHz in each zoom spectrum. We chose the broad band mode, as the lines in Sgr B2 are wide, so that the 0.27 MHz channels, corresponding to around 1.6 to 2.7 km s^{-1}, are quite adequate to resolve their structure. This mode also allowed a complete line-mapping survey to be made, without pre-selecting which lines would be covered, or the restrictions of selecting at most four lines in each 2.2 GHz sub-band.

The Mopra receiver covers the range 30 to 50 GHz in the so-called 7-mm band, so the band actually covers wavelengths 6 to 10 mm. We chose three tunings centred at 45.7, 38.0 and 34.1 GHz, to cover the range whole 30 to 50 GHz range. The latter two tunings overlap, with two 2.2 GHz sub-bands in common in the range 34 to 38 GHz.

The area was observed with on-the-fly (OTF) mapping, in an area 6×6 $arcmin^2$, centred near Sgr B2 (N) and (M), in a similar way to that described in Jones et al. (2008a). However, unlike the 3-mm imaging of Jones et al. (2008a), we used galactic coordinates for the scan direction, and hence square scan area. We used position switching for bandpass calibration with the off-source reference position observed before each 6 arcmin long source scan. The system temperature was calibrated with a noise diode. The 7-mm Mopra system does not use paddle scans (unlike the 3-mm system), and hence does not correct for the absorption through the atmosphere. This effect on calibration is around the 10 percent level, so we take that as the major uncertainty in the data.

The OTF data were turned into FITS data cubes with the LIVEDATA and GRIDZILLA packages[1]. The raw data files in RPFITS[2] format, were bandpass corrected using the off-source reference spectra with LIVEDATA, a robust second order polynomial fitted to the baseline and subtracted, and the data output as SDFITS (Garwood 2000) spectra. These spectra were then gridded into datacubes using GRIDZILLA, with a median filter for the interpolation. The median was used, as this is much more robust to the effect of bad data.

The whole 8-GHz band for each tuning was first turned into four cubes with frequency pixels for the 2.2-GHz sub-bands, making twelve cubes overall covering the entire 30 to 50 GHz range. These were used to conduct a full line survey in this spectral range. We identified a list of the strongest lines, as given in Table 1.

The GRIDZILLA scripts also allowed the lines (Table 1) to be specfied, with their rest frequencies, so that the GRIDZILLA output provides FITS cubes with velocity coordinates. We used this for a second pass through the data, to produce individual cubes for each line, over a velocity range -300 to 300 km s^{-1}. For the data over the frequency range 34 to 38 GHz, where two of the tunings overlapped, we combined the data from both observations to improve the signal-to-noise..

The FITS cubes were then read into the MIRIAD (Sault, Teuben, & Wright 1995) package for further processing and analysis. As the emission is typically of low surface brightness, the data were smoothed in velocity, with a 3-point hanning kernel, to make data cubes with improved surface brightness sensitivity. This gives around 0.54 MHz, or 3.2 to 5.4 km s^{-1} effective spectral resolution (across the spectral range), and ensures the data are Nyquist sampled in velocity.

The resolution of the Mopra beam in the 7-mm band was recently measured by Urquhart et al. (2010) to vary between 0.99 arcmin at 49 GHz and 1.37 arcmin at 31 GHz, or roughly $\theta = \lambda/D$ (where D is the 22-m dish diameter). We will assume these values to give resolution between 1.0 arcmin at 50 GHz, and 1.4 arcmin at 30 GHz, with the caveats that: a) this is somewhat smaller than previously quoted in the Mopra documentation as 82 arcsec (1.37 arcmin) at 42 GHz[3], and; b) actually gives a somewhat flatter variation than expected from $\theta \propto \lambda$. Since we are mostly concerned in this paper with the spatial and velocity structure, we have left the intensities in the T_A^* scale, without correction for the main beam efficiency onto the T_{MB} scale. The measured main beam efficiencies η_{mb} vary between 43

[1] http://www.atnf.csiro.au/people/mcalabre/livedata.html
[2] http://www.atnf.csiro.au/computing/software/rpfits.html
[3] http://www.narrabri.atnf.csiro.au/mopra/obsinfo.html

and 53 percent within the range 31 to 49 GHz, and extended beam efficiencies η_{xb} 56 to 69 percent (Urquhart et al. 2010)

3 RESULTS

We have produced data cubes for the 47 of the strongest lines in the 30 to 50 GHz range, as listed in Table 1. The flag in the last column of Table 1 refers to the source of the line identification. Most are from the NIST database[4] of lines known in the interstellar medium (Lovas & Dragoset 2004). As Sgr B2 is among the richest known sources of interstellar lines, these lines are mostly already well-known in Sgr B2. There are also some radio recombination lines, taken from the splatalogue compilation[5]. We have identified several lines in the JPL database[6] (Pickett et al. 1998) corresponding to other transitions of molecules (CH_2NH, NH_2CHO, NH_2CN, CH_3CHO) known in Sgr B2 from other frequencies, notably in the 3-mm band in Jones et al. (2008a).

The RMS noise in the (Hanning smoothed) data cubes varies from 34 to 76 mK (T_A^*).

There are also a few other weaker lines detected (mostly at the Sgr B2 (N) and (M) cores), but as they are quite weak and we do not have confident line identifications, we not consider them further here. Other projects are in progress to obtain line survey data for Sgr B2, notably the PRIMOS[7] survey with the 100-m Green Bank Telescope (GBT) of Sgr B2 (N) which will cover this 7-mm band (Remijan et al. 2008). These line surveys have longer integration time and higher sensitivity, and are better for studying the weak lines in the cores than the mapping observations presented here.

To study the spatial distribution of the different lines, we have made integrated emission images (Figs. 1 and 3 to 6). We integrated each data cube over a velocity range which included significant emission (above around 3 σ in the cubes) for each line, which means the velocity range is different for each line.

The integrated images in Figs. 1 and 3 to 6 are plotted as grey-scale, with the scale bar to the right in K km s^{-1} (T_A^*). The contour levels are in equal linear steps, mostly 2 K km s^{-1}, but sometimes 5 or 10 K km s^{-1}, and 100 K km s^{-1} for the very strong CH_3OH maser line at 36.17 GHz. We plot as fiducial marks the positions of radio sources as crosses and mid-IR sources as squares, as in Jones et al. (2008a). As the axes of Figs. 1 to 6 are Galactic coordinates, the north-south line of cores Sgr B2 (N), (M) and (S) is at a (Galactic) position angle around 45 degrees, with Sgr B2 (N) being the cross (radio source) near the centre at $l = 0.680$ deg., $b = -0.028$ deg., Sgr B2 (M) being the cross and square (radio and infrared source) below and to the right at $l = 0.667$ deg., $b = -0.036$ deg. and Sgr B2 (S) the cross and square further below and to the right at $l = 0.657$ deg., $b = -0.041$ deg. The radio and infrared peaks are plotted (with the N, M and S labels) in Fig. A1 in equatorial coordinates.

Table 1. Summary of strong lines detected in the Mopra observations. The first column gives an approximate frequency we have used for labelling transitions in this paper. The second column identifies the species, and the third its transition. The last columns indicates the rest frequency and the database used for the identification: L, Lovas: S, splatalogue; J, JPL (see text). The rest frequencies with a * indicate the frequency used for lines corresponding to multiple transitions, most also indicated as group (gp) in the transition list.

Rough Freq. GHz	line ID molecule or atom	transition	Exact Rest Freq. MHz	
30.00	SO	1(0) – 0(1)	30001.547	L
31.22	H	59 α	31223.313	S
31.95	HC_5N	12 – 11	31951.777	L
32.85	H	58 α	32852.196	S
33.75	CCS	3,2 – 2,1	33751.370	L
34.60	H	57 α	34596.383	S
34.61	HC_5N	13 – 12	34614.385	L
35.07	CH_2NH	3(0,3) – 2(1,2) gp	35065.545*	J
35.27	$H^{13}CCCN$	4 – 3 group	35267.440*	L
36.17	CH_3OH	4(−1,4) – 3(0,3) E	36169.290	L
36.39	HC_3N	4 – 3 group	36392.365*	L
36.47	H	56 α	36466.26	S
36.49	OCS	3 – 2	36488.813	L
36.80	CH_3CN	2(0) – 1(0) gp	36795.568*	L
37.28	HC_5N	14 – 13	37276.985	L
38.47	H	55 α	38473.358	S
38.506	CH_3CHO	2(0,2) – 1(0,1) E	38506.035	L
38.512	CH_3CHO	2(0,2) – 1(0,1) A	38512.081	L
39.36	CH_3CHO	2(1,1) – 1(1,0) E	39362.533	J
39.59	CH_3CHO	2(1,1) – 1(1,0) A	39594.292	J
39.73	NH_2CN	2(1,2) – 1(1,1),v=0	39725.3811	J
39.94	HC_5N	15 – 14	39939.574	L
40.25	CH_2CN	2 – 1 group	40253.884*	L
40.63	H	54 α	40630.498	S
40.88	NH_2CHO	2(1,2) – 1(1,1) gp	40875.2766*	J
42.39	NH_2CHO	2(0,2) – 1(0,1) gp	42386.070*	J
42.60	HC_5N	16 – 15	42602.153	L
42.67	HCS^+	1 – 0	42674.197	L
42.77	$HOCO^+$	2(0,2) – 1(0,1)	42766.1975	L
42.88	^{29}SiO	1 – 0 v=0	42879.922	L
42.95	H	53 α	42951.968	S
43.42	SiO	1 – 0 v=0	43423.864	L
43.96	HNCO	2(0,2) – 1(0,1) gp	43962.998*	L
44.07	CH_3OH	7(0,7) – 6(1,6) A+	44069.476	L
44.08	$H^{13}CCCN$	5 – 4	44084.172	L
45.26	HC_5N	17 – 16	45264.720	L
45.30	$HC^{13}CCN$	5 – 4	45297.346	L
	$HCC^{13}CN$	5 – 4	45301.707*	L
45.38	CCS	4,3 – 3,2	45379.029	L
45.45	H	52 α	45453.719	S
45.49	HC_3N	5 – 4 group	45490.316*	L
46.25	^{13}CS	1 – 0	46247.580	L
47.93	HC_5N	18 – 17	47927.275	L
48.15	H	51 α	48153.597	S
48.21	$C^{34}S$	1 – 0	48206.946	L
48.37	CH_3OH	1(0,1) – 0(0,0) A+	48372.467*	L
	CH_3OH	1(0,1) – 0(0,0) E	48376.889	L
48.65	OCS	4 – 3	48651.6043	L
48.99	CS	1 – 0	48990.957	L

[4] http://physics.nist.gov/PhysRefData/Micro/Html/contents.html
[5] http://www.splatalogue.net/
[6] http://spec.jpl.nasa.gov/ftp/pub/catalog/catform.html
[7] http://www.cv.nrao.edu/ aremijan/PRIMOS

Table 2. Summary of peaks fitted to the lines. The lines are grouped into the same order as plotted in Figs. 1 and 3 to 6. The positions are the fits to the maximum in the channel of strongest emission, and the velocity centre, velocity width (FWHM) and peak are from gaussian fits at the brightest pixel of the line emission. Note that the velocity centres use the rest frequencies from Table 1 so will be confused for the groups of lines, and the velocity widths will be increased for such confused lines.

line ID molecule or atom	Rest Freq. GHz	lat. peak deg.	long. peak deg.	veloc. centre km s^{-1}	veloc. width km s^{-1}	Peak T_A^* K
H 59 α	31.22	0.675	-0.031	62	48	0.40
H 58 α	32.85	0.674	-0.034	65	38	0.45
H 57 α	34.60	0.672	-0.035	64	34	0.46
H 56 α	36.47	0.676	-0.034	65	36	0.40
H 55 α	38.47	0.674	-0.035	65	34	0.43
H 54 α	40.63	0.672	-0.036	62	46	0.40
H 53 α	42.95	0.670	-0.034	67	35	0.33
H 52 α	45.45	0.672	-0.034	63	32	0.33
H 51 α	48.15	0.675	-0.034	64	54	0.39
HC_3N	36.39	0.692	-0.021	65	31	2.58
HC_3N	45.49	0.691	-0.022	66	30	2.17
$HCC^{13}CN$	45.30	0.682	-0.018	84	43	0.17
$H^{13}CCCN$	35.27	0.694	-0.010	65	25	0.20
$H^{13}CCCN$	44.08	0.679	-0.019	69	26	0.19
HC_5N	31.95	0.699	-0.022	65	24	0.29
HC_5N	34.61	0.691	-0.015	65	21	0.33
HC_5N	37.28	0.685	-0.010	67	22	0.31
HC_5N	39.94	0.675	-0.015	68	21	0.34
HC_5N	42.60	0.688	-0.021	69	20	0.32
HC_5N	45.26	0.698	-0.024	64	21	0.27
HC_5N	47.93	0.696	-0.025	65	25	0.39
CH_3OH	36.17	0.693	-0.024	67	22	35.7
CH_3OH	44.07	0.672	-0.028	65	21	1.77
CH_3OH	48.37	0.689	-0.022	64	35	2.59
CH_3CHO	38.506	0.687	-0.014	70	26	0.26
CH_3CHO	38.512	0.679	-0.007	64	39	0.22
CH_3CHO	39.36	0.687	-0.021	70	18	0.16
CH_3CHO	39.59	0.684	-0.012	68	20	0.21
NH_2CHO	40.88	0.684	-0.008	64	18	0.21
NH_2CHO	42.39	0.681	-0.012	70	25	0.24
SO [1]	30.00	0.695	-0.008	58	(25)	0.26
SiO	43.42	0.707	-0.021	57	50	0.67
^{29}SiO	42.88	0.673	-0.009	67	25	0.14
CS [2]	48.99	0.664	-0.040	51	11	1.91
				83	26	1.39
^{13}CS	46.25	0.656	-0.041	60	25	0.31
$C^{34}S$	48.21	0.662	-0.042	61	33	0.45
CCS	33.75	0.693	-0.020	66	24	0.27
CCS	45.38	0.683	-0.008	65	18	0.24
CH_3CN	36.80	0.680	-0.012	72	33	0.71
OCS	36.49	0.676	-0.032	63	20	0.47
OCS	48.65	0.692	-0.024	62	25	0.52
HNCO	43.96	0.696	-0.021	64	24	2.30
$HOCO^+$	42.77	0.682	-0.011	67	20	0.34
CH_2NH	35.07	0.668	-0.034	60	20	0.48
NH_2CN	39.73	0.699	-0.024	67	47	0.20
HCS^+	42.67	0.674	-0.011	66	19	0.17
CH_2CN	40.25	0.651	-0.055	54	69	0.21

[1] SO line at band edge, fitted with fixed width, due to poor data
[2] CS line with self-absorption, fitted as two gaussians

We discuss these images in more detail below, in subsections 3.1 to 3.14.

For quantitative analysis of the differences in spatial distribution of the different lines, we have fitted the position of the peak emission in the data cubes, with the MIRIAD task *maxfit*, which fits the position with a parabolic fit to the spatial pixels around the peak pixel in the cube. This is similar to the analysis used in Jones et al. (2008a) for the 3-mm Sgr B2 Mopra imaging, but we only fit the strongest peak, not multiple peaks, as the resolution is lower here at 7 mm and much of the spatial structure is merged together. As the emission is typically complex and extended, we do not generally fit the spatial structure as gaussian peaks.

These peak positions are tabulated in Table 2, arranged in groups of similar lines, as plotted in Figs. 1 and 3 to 6. We note that due to absorption in some of the spectra, and line width differences across the area, that the position of the peak emission in the data cubes is not the same as the position of the peak of integrated emission.

The velocity structure was studied by fitting the spectrum in each data cube at the position of the pixel of strongest emission, with the MIRIAD task *gaufit*. The fitted velocity and velocity width are given in Table 2. The peak brightness (T_A^*) at this position is also listed, to give an indication of line strength. We have used the hanning smoothed data cubes, with spectral resolution 3.2 to 5.4 km s^{-1}, for the fitting, but this is not expected to significantly affect the velocity widths.

3.1 Hydrogen recombination lines

There are nine radio recombination lines (RRLs) of hydrogen, in the series H 51 α to H 59 α, shown in Fig. 1. They peak between the two strong free-free radio continuum sources Sgr B2 (N) and (M), with both sources contributing to the RRL emission. The mean peak position for the nine lines (Table 2) is $l = 0.673$ deg., $b = -0.034$ deg., mean velocity 64 km s^{-1} and mean velocity width 40 km s^{-1}.

We show in Fig. 2 the peak positions of the RRLs relative to (our previously unpublished) higher resolution Australia Telescope Compact Array (ATCA) observations of the continuum. The low resolution Mopra data merge together the RRL emission from Sgr B2 (N) and (M). We also note (see the Appendix) that the 7-mm free-free emission has an extended diffuse component, in addition to the cores Sgr B2 (N) and (M), which is resolved out in the ATCA observations. The extended component contributes close to half of the radio flux in this 30 to 50 GHz range.

For comparison BIMA observations of H 59 α RRL in both Sgr B2 (M) and (N) are given in Pei, Liu, & Snyder (2000) and higher resolution VLA observations of the H 52 α in Sgr B2 (M) are given by de Pree et al. (1996).

The 7-mm free-free emission probed by the RRLs and shown in Fig. 2 also indicates where there may be absorption of molecular lines (Figs. 3 to 6) by the strong Sgr B2 (N) and (M) continuum.

3.2 HC_3N and ^{13}C isotopologues

There are two lines of cyanoacetylene HC_3N, shown in Fig. 3, the 4–3 (36.39 GHz) and 5–4 (45.49 GHz) groups of transitions. The integrated emission is distributed on a ridge

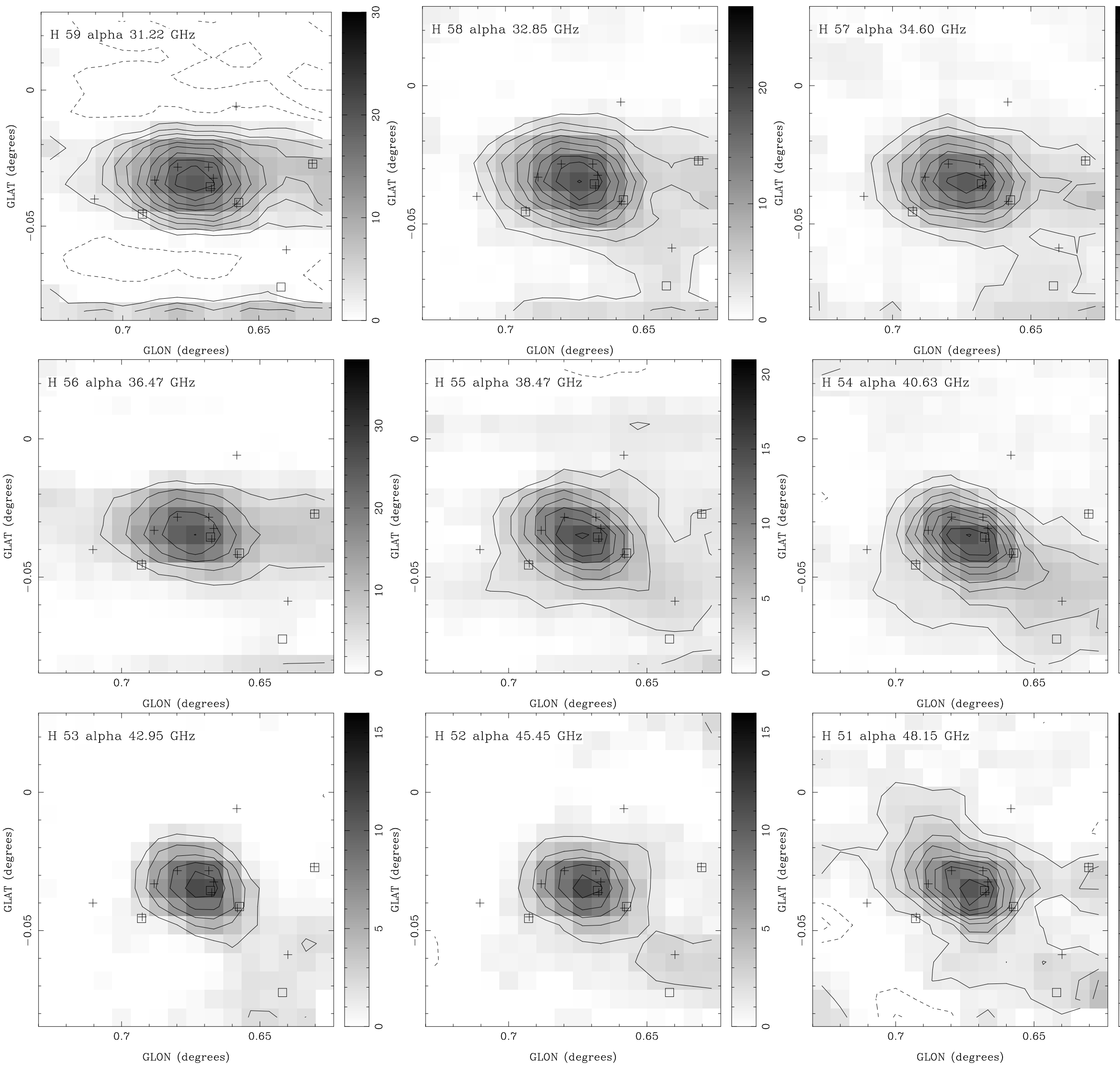

Figure 1. The integrated emission images for the nine lines of hydrogen recombination H 59 α to H 51 α. In this figure and later images the crosses (+) denote the position of radio peaks and the open squares (□) positions of infrared peaks. The line of cores Sgr B2 (N), (M) and (S) is at a (Galactic) position angle around 45 degrees, with Sgr B2 (N) being the cross near the centre at $l = 0.680$ deg., $b = -0.028$ deg., Sgr B2 (M) being the cross and square below and to the right at $l = 0.667$ deg., $b = -0.036$ deg. and Sgr B2 (S) the cross and square further below and to the right at $l = 0.657$ deg., $b = -0.041$ deg. The scale bar is in units of K km s_{-1}, for $\int T_A^* dv$.

at higher latitudes than the Sgr B2 (N), (M) and (S) line (shown as crosses), that is to the north-west in equatorial coordinates, with the peak to the north of Sgr B2 (N). This is similar to the distribution of the HC_3N 3-mm lines 9–8, 10–9, 11–10 and 12–11 found in Jones et al. (2008a). It is also similar to the distribution of the 4–3 line in Lis & Goldsmith (1991) and Chung, Ohishi, & Morimoto (1994), but these latter data covered smaller areas.

There are also three lines of the ^{13}C isotopologues of HC_3N, the combined $HCC^{13}CN$ and $HCC^{13}CN$ 5–4 line (45.30 GHz), the $H^{13}CCCN$ 4–3 (35.27 GHz) and $H^{13}CCCN$ 5–4 (44.08 GHz) lines. These are all quite weak lines, but the 45.30 GHz line shows good agreement in spatial distribution to the HC_3N lines. The other two show fair agreement, but may be affected by scanning artifacts, with stripes along the longitude direction.

The mean peak position for the five lines is $l = 0.688$ deg., $b = -0.018$ deg., and, for the four lines not blended, mean velocity 66 km s^{-1} and mean velocity width 28 km s^{-1}. (Note that the blended 45.30 GHz line has larger width, and anomalous velocity, in Table 2.)

3.3 HC_5N

There are seven lines of cyanodiacetylene HC_5N, shown in Fig. 3, the series from 12–11 (31.95 GHz) to 18–17 (47.93 GHz) transitions. The lines are all quite weak, but the distribution is similar to that of HC_3N (above), best seen in the

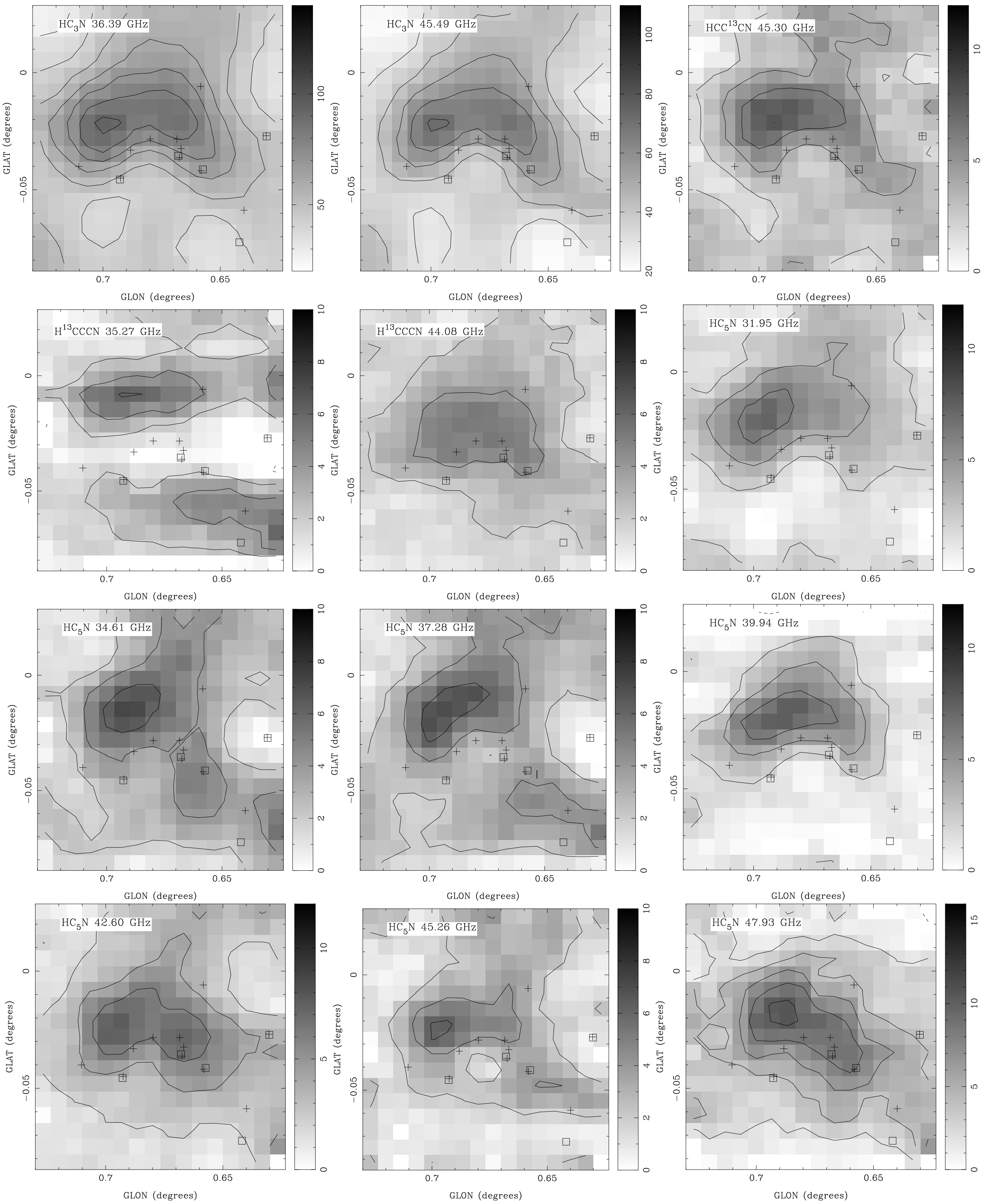

Figure 3. The integrated emission images for two lines of HC_3N, three lines of ^{13}C isotoplogues of HC_3N, and seven lines of HC_5N.

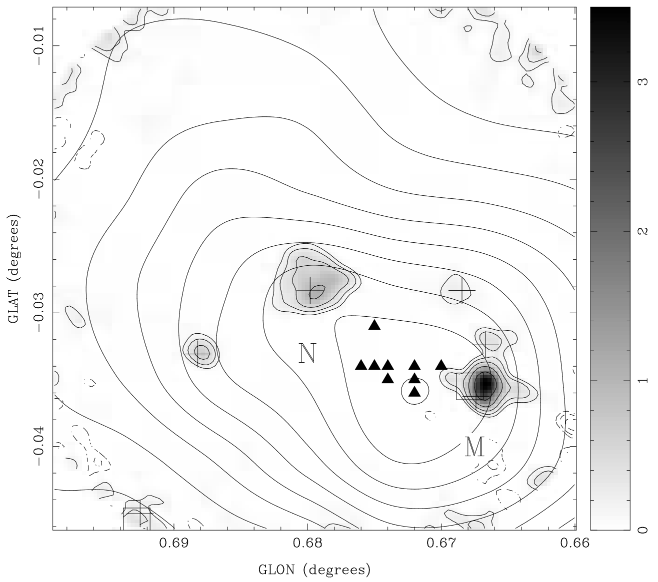

Figure 2. The fitted peak positions of the 7-mm radio recombination lines (filled) triangles, relative to the high resolution 7-mm radio continuum emission, from ATCA observations, in grey-scale and contours, with the low resolution Mopra integrated H 51 α also plotted as contours. The recombination lines include emission from Sgr B2 (N), centre, Sgr B2 (M), lower right, and the extended envelope resolved out in the ATCA data.

31.95 GHz and 39.94 GHz lines, but broadly similar in the other lines, with the ridge to more positive latitudes than the radio sources (crosses). The mean peak position for the seven lines is $l = 0.690$ deg., $b = -0.019$ deg., mean velocity 66 km s^{-1} and mean velocity width 22 km s^{-1}.

3.4 CH_3OH

There are three lines of methanol CH_3OH, shown in Fig. 4, the 4(−1,4) – 3(0,3) E (36.17 GHz), 7(0,7) – 6(1,6) A+ (44.07 GHz) and the 1(0,1) – 0(0,0) A+ plus 1(0,1) – 0(0,0) E (48.37 GHz) lines. The three line have quite different distributions, due to the complex collisional and radiative excitation processes of methanol.

The 36.17 GHz line can act as a (class I) maser, which gives the high brightness peak seen here in Fig. 4. Note that the peak is at the north cloud (Jones et al. 2008a) at $l = 0.693$ deg., $b = -0.024$ deg. The distribution is in good agreement with that found by Liechti & Wilson (1996) for this line, with higher resolution Effelsberg 100-m telescope observations.

The 44.07 GHz line can also act as a (class I) maser. Mehringer & Menten (1997) have used the VLA at much higher resolution than the Mopra data here to map the distribution of this line. They find many maser and quasi-thermal peaks near the Sgr B2 (N) and (M) cores. The Mopra data (Fig. 4) are consistent with this distribution.

The 48.37 GHz line has a distribution that is similar to HC_3N (Fig. 3) and other 3-mm transitions of methanol in Jones et al. (2008a). This is not a maser transition so comparison with the 44.07 GHz line is instructive (Val'tts et al. 1991).

3.5 CH_3CHO

There are four lines of acetaldehyde CH_3CHO, shown in Fig. 4, the 2(0,2) – 1(0,1) E (38.506 GHz), 2(0,2) – 1(0,1) A (38.512 GHz), 2(1,1) – 1(1,0) E (39.36 GHz) and 2(1,1) – 1(1,0) A (39.59 GHz) lines.

The distribution of integrated emission from acetaldehyde is widespread, as found by Chengalur & Kanekar (2003). However, we find for these 7-mm lines that there is a deficit of emission near Sgr B2 (N) and (M), probably due to absorption. Chengalur & Kanekar (2003) find the 1(1,1) – 1(1,0) transition at 1065 MHz in emission near Sgr B2 (N), (M) and (S), which they attribute to a weak maser. The distribution of the four lines is similar, although the 39.36 and 39.59 GHz lines are weak. The emission peaks at the north cloud with mean peak position $l = 0.684$ deg., $b = -0.014$ deg., mean velocity 68 km s^{-1} and mean velocity width 26 km s^{-1}.

3.6 NH_2CHO

There are two lines of formamide NH_2CHO, shown in Fig. 4, the 2(1,2) – 1(1,1) group (40.88 GHz) and the 2(0,2) – 1(0,1) group (42.39 GHz). The distribution of integrated emission is similar to that of acetaldehyde (above) with widespread emission, peaking at the north cloud (mean peak position $l = 0.683$ deg., $b = -0.010$ deg.) and a deficit near Sgr B2 (N) and (M). This distribution is somewhat different to that of the formamide 5(1,4) – 4(1,4) line at 102.07 GHz in Jones et al. (2008a) which peaks on the ridge to the west of Sgr B2 (M), but this line is confused with the protonated formaldehyde H_2COH^+ 4(0,4) – 3(1,3) line (Ohishi et al. 1996).

3.7 SO

There is one line of sulphur monoxide SO, shown in Fig. 5, the 1(0) – 0(1) (30.00 GHz) line. There is widespread emission over the area, with strong absorption near Sgr B2 (M). This is in contrast to the 3-mm SO lines, where the emission is strongly peaked at Sgr B2 (M) in the 2(2) – 1(1) (86.09 GHz) and 2(3) – 1(2) (109.25 GHz) lines, and extended along the ridge-line to the west of Sgr B2 (M) in the 3(2) – 2(1) (99.30 GHz) line (Jones et al. 2008a; Goldsmith et al. 1987).

3.8 SiO and ^{29}SiO

There are two lines of silicon monoxide SiO 1 – 0 v=0 (43.42 GHz), and the isotopologue ^{29}SiO 1 – 0 v=0 (42.88 GHz) shown in Fig. 5. The integrated emission is widely distributed in both lines, with absorption near Sgr B2 (M) and (N), like the SO line (above). The ratio between the isotopologue ^{29}SiO and SiO, indicates that the SiO is optically thick. This leads to the differences in the integrated distribution, and fitted mean velocity and velocity width in Table 2, as the suppression of emission in the SiO line centre shifts the mean and increases the fitted width. The SiO 1 – 0 line distribution coincides with the peak labelled SiO+69-0.06 of this line in Martin-Pintado et al. (1997), and has similar absorption at Sgr B2 (M) and (N) seen in the 3-mm SiO 2 – 1 (86.85 GHz) line in that paper. It is also similar to the

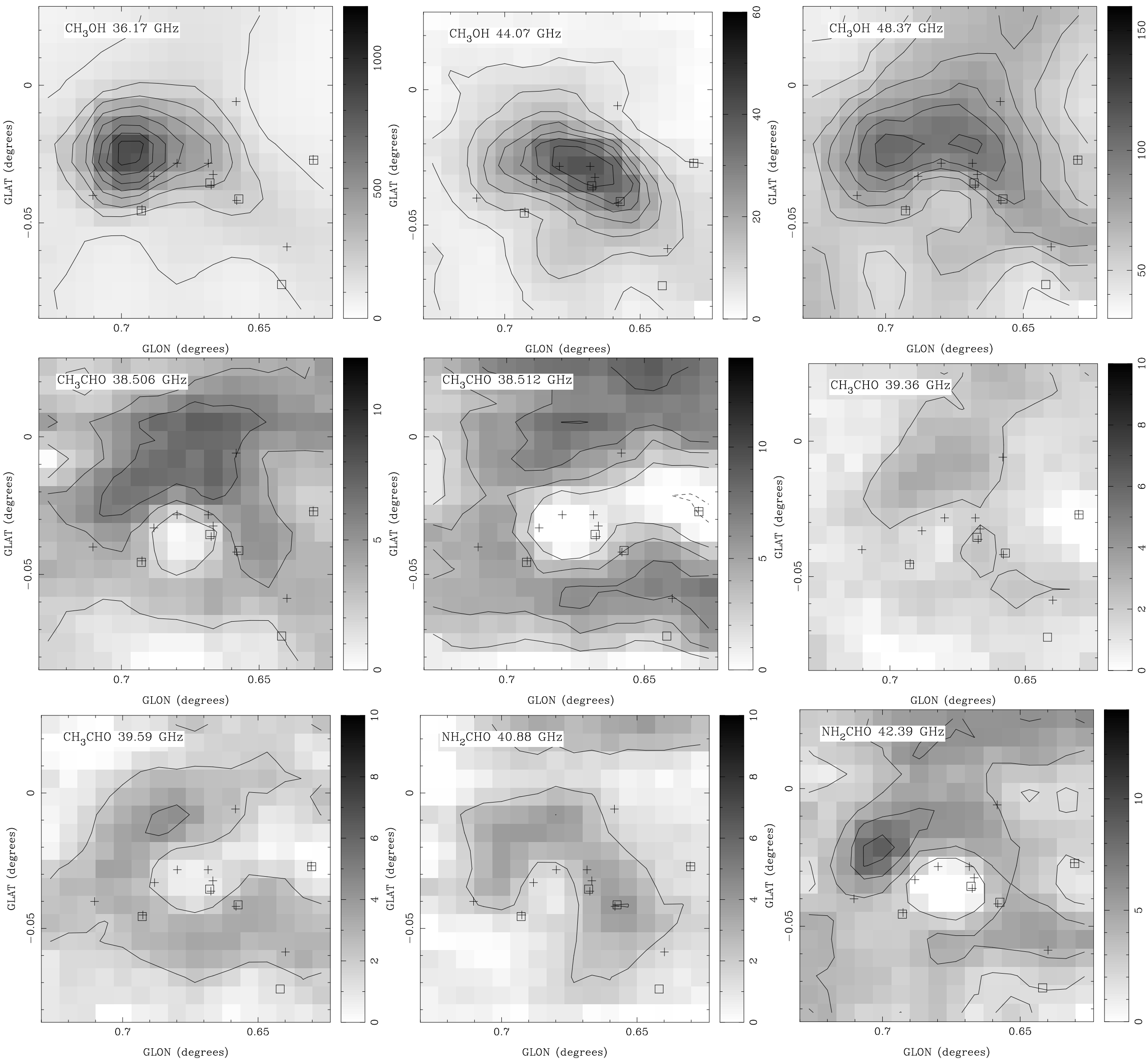

Figure 4. The integrated emission images for three lines of CH_3OH (methanol), four lines of CH_3CHO and two lines of NH_2CHO.

distribution of the SiO 2 – 1 line in Minh (2007) and Jones et al. (2008a), but the latter is at lower signal to noise.

We also have data for the maser lines SiO 1 – 0 v=1 (43.122 GHz) and 1 – 0 v=2 (42.821 GHz) but did not detect these lines above a 3 σ level of 0.10 K, although these lines have been detected in Sgr B2 by, for example Zapata et al. (2009). If the v=1 line was a strong as that reported by Zapata et al. (2009), corresponding to 0.18 K, it would have been detected here, but such masers are variable, so it is quite plausible that the strength has changed.

3.9 CS, ^{13}CS and C^{34}S

There are three lines of carbon monosulphide CS 1 – 0 (48.99 GHz) and the isotopologues ^{13}CS 1 – 0 (46.25 GHz) and C^{34}S 1 – 0 (48.21 GHz) shown in Fig. 5. Like the SiO line above, there is widespread emission, with absorption near Sgr B2 (M) and (N). There are optical depth effects which make the integrated emission of the CS line and the isotopologues ^{13}CS 1 – 0 and C^{34}S different. The peaks in the data cubes (Table 2) are near Sgr B2 (M) at peak position l = 0.661 deg., $b = -0.041$ deg. (mean of the five lines). The CS line shows absorption, so is fitted in Table 2 as two gaussians, offset in velocity. The peaks of integrated emission (Fig. 5) are at different positions, due to the effects of absorption. These distributions are similar to that found by Jones et al. (2008a) for the 3-mm lines CS 2 – 1 (97.98 GHz) and the isotopologues ^{13}CS 2 – 1 (92.49 GHz) and C^{34}S 2 – 1 (96.41 GHz). The CS 1 – 0 (48.99 GHz) line has also been mapped by Sato et al. (2000), with the Nobeyama 45-m telescope at higher resolution, showing similar line distribution.

3.10 CCS

There are two lines of dicarbon monosulphide CCS shown in Fig. 5, the 3,2 – 2,1 (33.75 GHz) and 4,3 – 3,2 (45.38

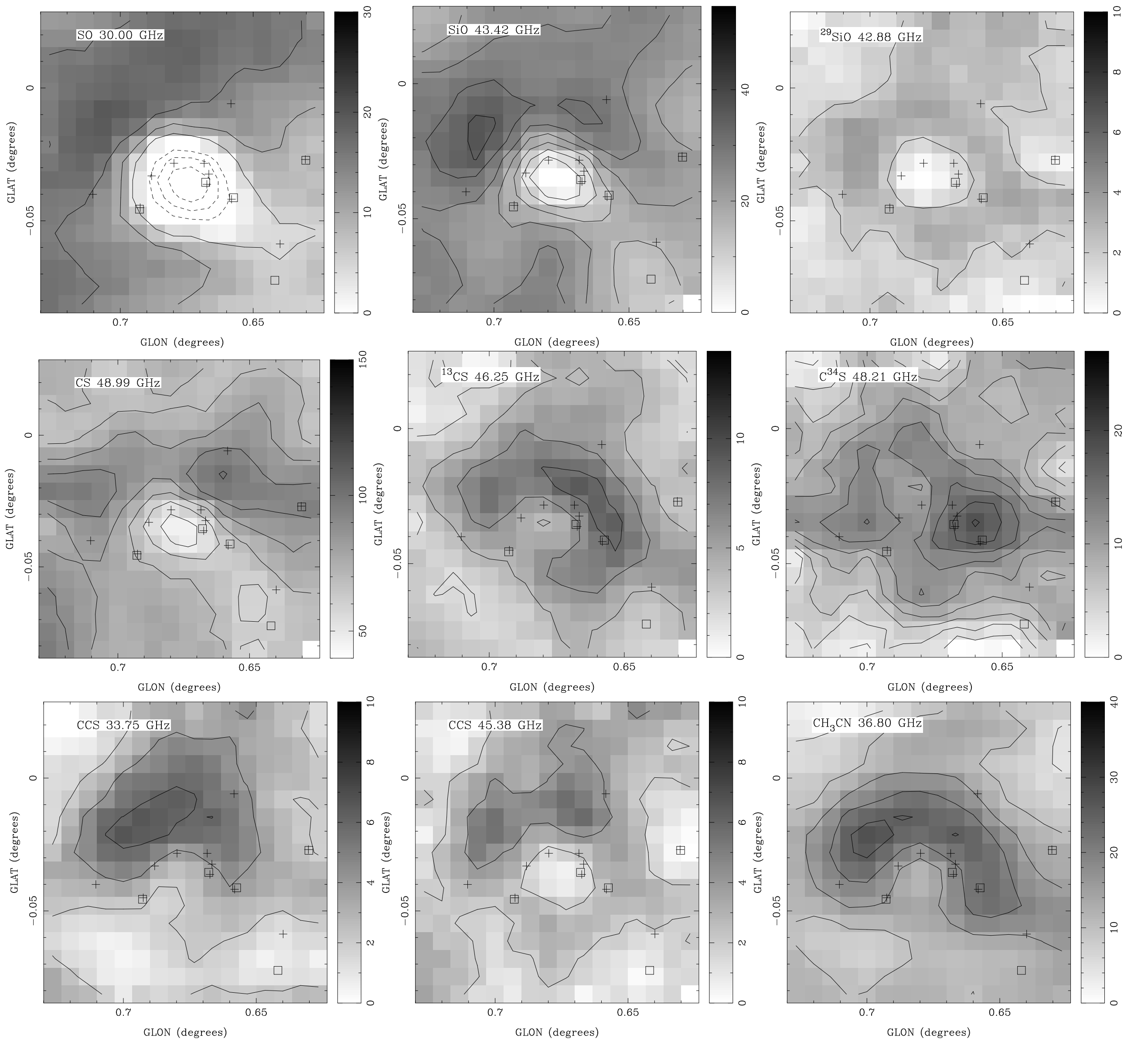

Figure 5. The integrated emission images for one line each of SO, SiO, ^{29}SiO, CS, ^{13}CS and C^{34}S, two lines of CCS and one line of CH_3CN. Note that the dashed contours indicate negative integrated emission, or absorption.

GHz) lines. The emission peaks in the north cloud, with mean peak position $l = 0.688$ deg., $b = -0.014$ deg., mean velocity 66 km s^{-1} and mean velocity width 21 km s^{-1}. The integrated emission avoids the Sgr B2 (M) and (N) area, but this may be due to absorption, as shown in the CCS 45.38 GHz line (Fig 5). This is different to the distribution of the CCS 7,6 – 6,5 (81.505 GHz) line shown by Kuan & Snyder (1994), at higher resolution, which peaks near Sgr B2 (M) and (S).

3.11 CH_3CN

There is one line of methyl cyanide CH_3CN, shown in Fig. 5, the 2(0) – 1(0) group (36.80 GHz). The emission also peaks in the north cloud, and shows the ridge in the integrated emission to the north-west of Sgr B2 (N) and (M), similar to that in the CH_3CN 5 – 4 (91.99 GHz) and 6 – 5 (110.38 GHz) lines in Jones et al. (2008a) and the 5 – 4 line in de Vicente, Martin-Pintado, & Wilson (1997). There may also be some absorption in the 2(0) – 1(0) line here, around Sgr B2 (N) and (M), not just a deficit of emission.

3.12 OCS

There are two lines of carbonyl sulphide OCS shown in Fig. 6, the 3 – 2 (36.49 GHz) and 4 – 3 (48.65 GHz) lines. The emission peaks in the north cloud, with mean peak position $l = 0.684$ deg., $b = -0.028$ deg., mean velocity 63 km s^{-1} and mean velocity width 22 km s^{-1}, although there are some differences in distribution between the two transitions. The distribution is similar to the 7 – 6 (85.14 GHz), 8 – 7 (97.30 GHz) and 9 – 8 (109.46 GHz) lines (Jones et al. 2008a), with the ridge near Sgr B2 (N) and (M).

© 2010 RAS, MNRAS **000**, 1–18

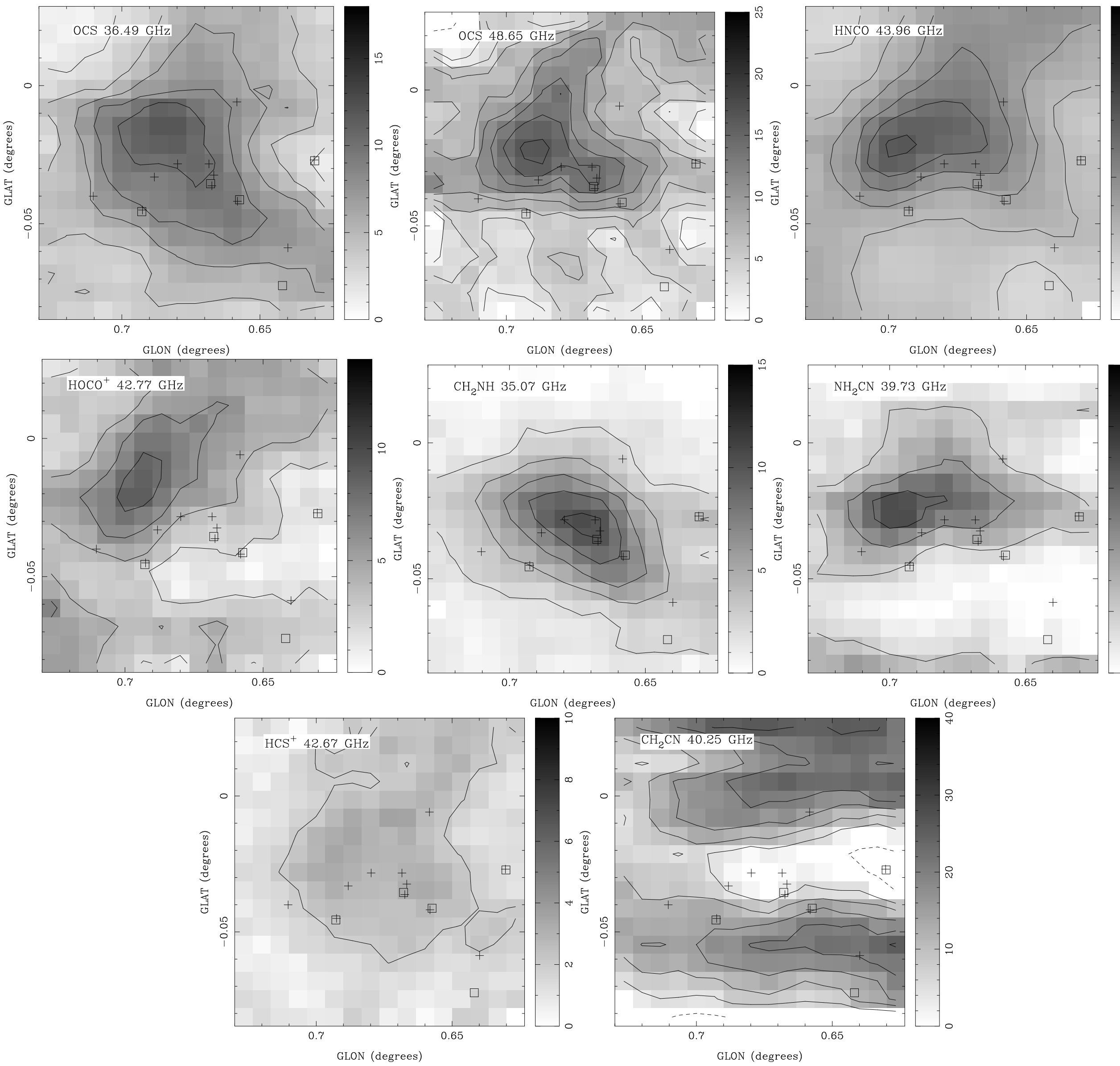

Figure 6. The integrated emission images for two lines of OCS, and one line each of HNCO, $HOCO^+$, CH_2NH, NH_2CN, HCS^+ and CH_2CN.

3.13 HNCO and $HOCO^+$

There is one line of isocyanic acid HNCO the 2(0,2) – 1(0,1) group (43.96 GHz) and one of protonated CO_2 $HOCO^+$ 2(0,2) – 1(0,1) (42.77 GHz) shown in Fig. 6. Both of these lines peak at the north cloud, so the molecules are discussed here together.

The HNCO 43.96 GHz distribution is similar to that of the 4(0,4) – 3(0,3) (87.93 GHz) and 5(0,5) – 4(0,4) (109.91 GHz) lines in Jones et al. (2008a) and Minh et al. (1998). Observations of the 4(0,4) – 3(0,3) line over a wider area (albeit at lower resolution) are shown in Minh & Irvine (2006) along with discussion of this north cloud (called the 2'N HNCO peak by them). There are also observations of the 1(0,1) – 0(0,0) (21.98 GHz) line in Wilson et al. (1996), with similar distribution.

The $HOCO^+$ 42.77 GHz distribution similar to that of the 4(0,4) – 3(0,3) (85.53 GHz) and 5(0,5) – 4(0,4) (106.91 GHz) lines in Jones et al. (2008a), Minh et al. (1998) and Minh, Irvine, & Ziurys (1988) and similar to the HNCO lines, highlighting the chemical distinctness of this north cloud (Wilson et al. 1996) from the Sgr B2 (M) and (N) area.

3.14 CH_2NH, NH_2CN, HCS^+ and CH_2CN

Finally, there is one line of each of the methylenimine CH_2NH 3(0,3) – 2(1,2) group (35.07 GHz), cyanamide NH_2CN 2(1,2) – 1(1,1),v=0 (39.73 GHz), thioformyl HCS^+ 1 – 0 (42.67 GHz) and the cyanomethyl radical CH_2CN 2 – 1 group (40.25 GHz) shown in Fig. 6.

The CH_2NH 35.07 GHz line distribution peaks near Sgr B2 (M), and is similar to the distribution of the 4(0,4) – 3(1,3) (105.79 GHz) line in Jones et al. (2008a). The latter being at higher resolution resolves the structure better, showing the peak at Sgr B2 (N) whereas the fitted peak in the 35.07 GHz line is near Sgr B2 (M). There are likely to be excitation differences between the two cores.

The NH_2CN 39.73 GHz line peaks at the north cloud, with the ridge to the north-west of Sgr B2 (M), with a distribution similar to that of the 5(1,4) – 4(1,3) (100.63 GHz) line (Jones et al. 2008a), although the image there is noisy and affected by scanning stripes.

The HCS^+ 42.67 GHz line is quite weak, but has an extended distribution. Not much is known on the distribution of this ion in Sgr B2, but it is plausible that the distribution is similar to that of CS (e.g. Fig. 5, subsection 3.9).

The distribution of integrated emission of the CH_2CN 40.25 GHz line is extended, with likely absorption near Sgr B2 (N). There are some stripes in the integrated emission in the longitude scanning direction. The distribution differs from that of CH_3CN (Fig. 5, subsection 3.11) which may indicate that the two molecules have quite different formation routes and destruction paths (Irvine et al. 1988; Turner et al. 1990) despite their apparent similarity.

3.15 Summary of peak positions

The peak positions of the 7-mm lines in the data cubes tabulated in Table 2 are plotted in Fig. 7. The hydrogen recombination lines (filled triangles in Fig. 7) peak between Sgr B2 (N) and (M), as discussed in subsection 3.1 and shown in Fig. 2. The molecular lines mostly peak at the north cloud.

We attribute the molecular line distributions in this 7-mm band to be a combination of the effect of emission, from an extended cloud centred to the east of Sgr B2 (N) and (M), and absorption due to the free-free continuum at Sgr B2 (N) and (M). We consider this further in the Discussion (Section 5) and in the next section (4) where we analyse the spatial distributions in a relatively objective way.

4 PRINCIPAL COMPONENT ANALYSIS

The integrated emission images of the different lines shown in Figs. 1 and 3 to 6 show similarities and differences. One useful technique to identify and quantify the features of large data sets is Principal Component Analysis (PCA), see e.g Heyer & Schloerb (1997). This describes the multi-dimensional data set by linear combinations of the data that describe the largest variance (the most significant common feature) and successively smaller variances (the next most significant features).

In the context here, we can use PCA to describe the large number of images, with a smaller set of images which contain the most significant features. This has been used by Ungerechts et al. (1997) for the OMC-1 ridge, and more recently by us for the G333 molecular cloud (Lo et al. 2009) and the Sgr B2 area with 3-mm molecular lines (Jones et al. 2008c).

We have implemented the PCA processing in a PYTHON script, with the PCA module[8], and pyFITS[9] to read and write the FITS images.

[8] http://folk.uio.no/henninri/pca_module/
[9] http://www.stsci.edu/resources/software_hardware/pyfits/

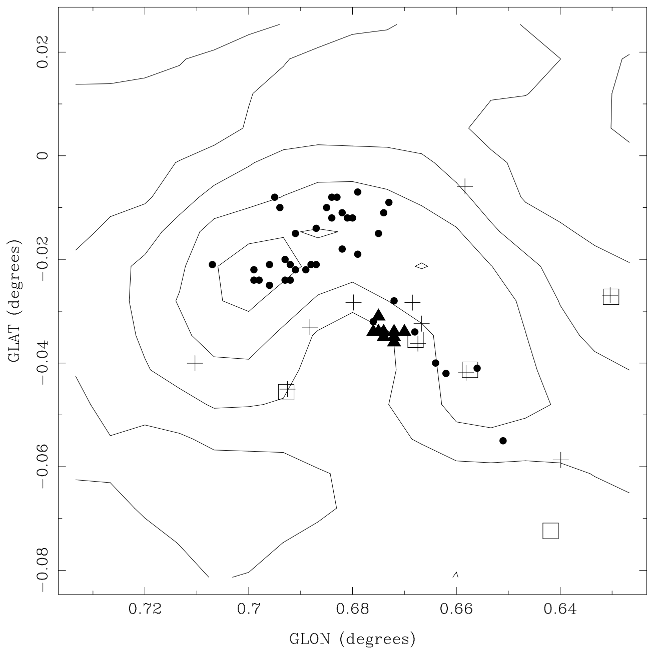

Figure 7. The positions of the fitted 7-mm peaks, with filled circles for the molecular peaks and filled triangles for the H radio recombination lines. The contours are from the CH_3CN line. The crosses are radio peaks and open squares infrared peaks, as in other images.

The images of the three most significant components of the 7-mm integrated emission are shown in Fig. 8. The first four components describe respectively 56, 14, 9 and 4 percent of the variance in the data. These components are statistical descriptions of the integrated line images, not necessarily physical components of Sgr B2. However, they do highlight the physical features in a useful way.

The first component (Fig. 8) highlights emission from the north cloud and ridge. The second component highlights absorption (or emission) from Sgr B2 (N) and (M), and also some differences in the north cloud. The third component highlights differences in emission to the south. The fourth component (not shown here in Fig. 8) highlights differences in emission from Sgr B2 (N).

The relations between the molecular integrated emission images, and the PCA images are shown in Fig. 9 as vectors of the projection of the data images on the axes of the PCA images. The molecules are labelled with numbers, for clarity, in these plots. All of the data images are positively correlated with the first PCA image, except for SO (37). The greatest positive correlation with the second PCA component are for SO (37) and SiO (36), which have strong absorption at Sgr B2 (N) and (M). The greatest negative correlation with the second PCA component are for CH_2NH (6) and the CH_3OH 44.07 GHz line (12), which have emission at Sgr B2 (N) and (M). The greatest positive correlation with the third PCA component are for the CH_3CHO 38.512 GHz line (7) and the $H^{13}CCCN$ 35.27 GHz line (17), and greatest negative correlation with the third PCA component are for NH_2CN (33) and CS (15), highlighting more or less emission to the south, relative to the other lines.

We used the integrated emission images for 37 molecules here in the PCA, excluding CH_2CN (as it is probably af-

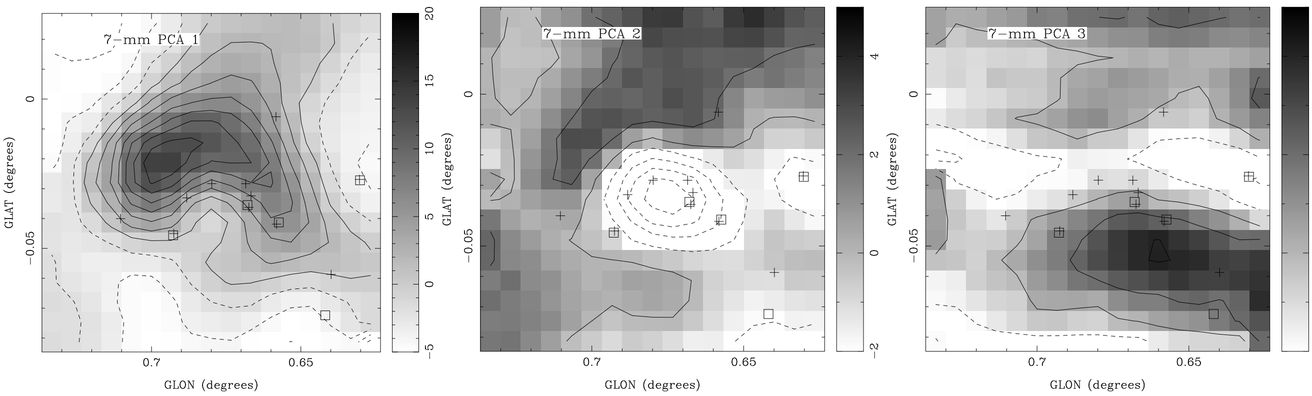

Figure 8. The first three images from the Principal Component Analysis (PCA) for the 7-mm lines, describing 56, 14 and 9 percent of the data variance respectively. The first image highlights emission from the north cloud and ridge, the second image highlights absorption (or emission) from Sgr B2 (N) and (M) and the third image highlights differences in emission to the south.

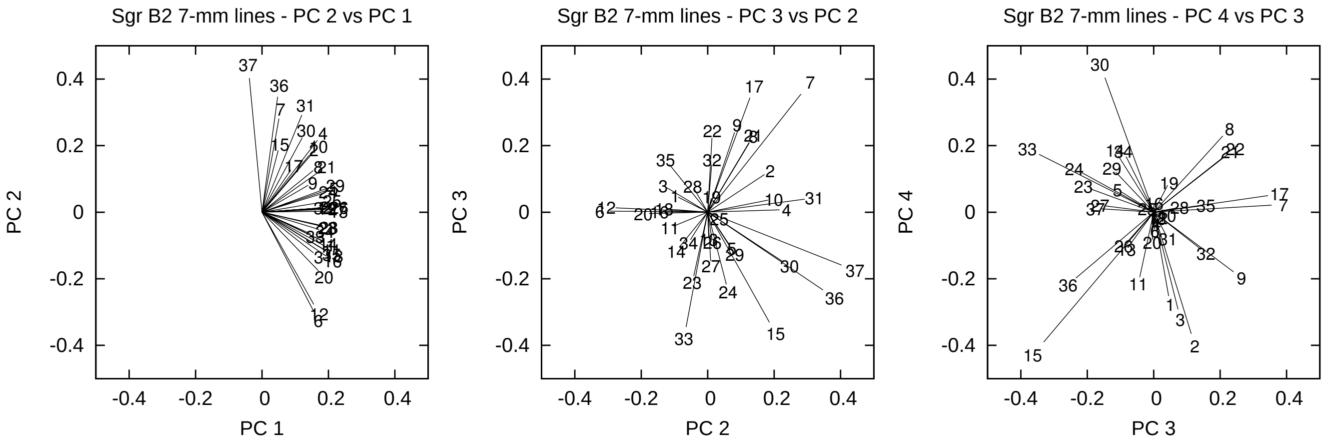

Figure 9. The component vectors of the integrated line images in the decomposition of the data into the PCA images, shown with successive pairs of PCA images. The vectors are labelled with numbers, rather than molecule names, for clarity of presentation, with the molecules listed in alphabetical order: 1, ^{13}CS; 2, ^{29}SiO;3, C^{34}S; 4 and 5, two lines of CCS; 6, CH_2NH; 7 to 10, four lines of CH_3CHO; 11, CH_3CN; 12 to 14, three lines of CH_3OH; 15, CS; 16 and 17, two lines of H^{13}CCCN; 18 to 24, seven lines of HC_5N; 25, HCC^{13}CN; 26 and 27, two lines of HC_3N; 28, HCS^+; 29, HNCO; 30, $HOCO^+$; 31 and 32, two lines of NH_2CHO; 33, NH_2CN; 34 and 35, two lines of OCS; 36, SiO, and; 37, SO.

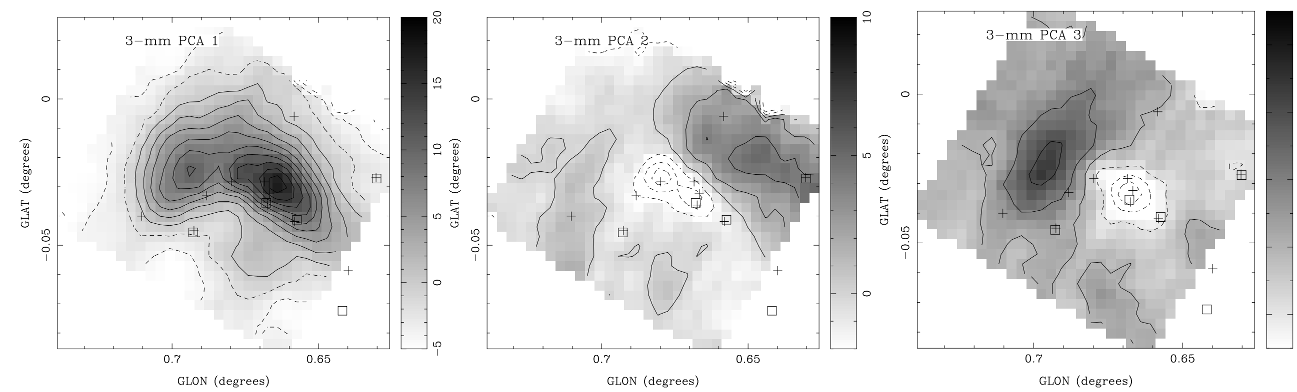

Figure 10. The first three images from the Principal Component Analysis (PCA) for the 3-mm lines (lower) from Jones et al. (2008a). These 3-mm images are similar to those in Jones et al. (2008c) rotated into Galactic coordinates for easier comparison to the 7-mm images. The first image highlights emission from the north cloud and ridge. The second image highlights absorption (or emission) from Sgr B2 (N) and (M) and emission from the south-west. The third image highlights the north cloud and differences in emission from Sgr B2 (M).

fected by the scanning ripples), and not including the radio recombination lines (RRLs), as they are due to a different physical mechanism. However, we have also calculated the PCA for the 46 integrated emission images, including the RRLs, and find very similar results. The first four components then describe respectively 49, 24, 8 and 3 percent of the variance in the data, with the PCA images quantitatively very similar, with the major difference being the second component image having a stronger peak at Sgr B2 (N) and (M), describing the RRLs, and positive rather than negative. However, the sign of the component images is not physically significant.

The PCA images from these Sgr B2 7-mm lines can be compared to those found for the Sgr B2 3-mm lines from Jones et al. (2008a) in Fig. 10 (Jones et al. 2008c). The 3-mm PCA images are at higher resolution.

The first two PCA component images are similar: the first highlighting the ridge and north cloud, and the second highlighting absorption at Sgr B2 (N) and (M). The second PCA component at 3-mm also includes emission to the south-west, as some of the strongest lines at 3-mm, such as HCN, HCO^+ and HNC are optically thick with both absorption at Sgr B2 (N) and (M) and the south-west area relativly stronger (as the the main emission is relatively weaker due to the high optical depth). The third 3-mm PCA component highlights the north cloud, and Sgr B2 (M). As PCA is a statistical tool, it is not expected that the higher PCA images, of lower statistical weight, should be the same from the independent 7-mm and 3-mm data. However, the PCA images from the 3-mm and 7-mm data do show quite similar spatial features, albeit distributed differently amongst the PCA images: ridge, north cloud, Sgr B2 (N) and Sgr B2 (M).

5 DISCUSSION

We can consider the distribution of the spectral lines in terms of physical components of the Sgr B2 complex. These are related to the Principal Components discussed in the last section, but are not the same decomposition of structure into features. In Jones et al. (2008a) we identified seven features. Of these, the extended ridge and north cloud are related to the extended envelope of Sgr B2 (Jones et al. 2008a) which is traced by the dust seen at sub-mm wavelengths (Fig. A1). The hot cores Sgr B2 (N), (M) and (S) are denser and warmer, and so have different chemistry, so they are prominent in particular molecules, as shown in Fig. 6 by CH_2NH. In the 7-mm band data here, there is also often absorption in the area around Sgr B2 (N) and (M) related to the radiative transfer of the continuum free-free emission through the molecular gas.

To better describe the quantitative properties of these physical components of Sgr B2, we have considered in the Appendix continuum data (imaging and photometry) from the radio, through sub-mm to mid-IR wavelenths, from the literature, plus some of our own (as yet unpublished) radio and sub-mm data, and data from public archives. We have fitted the spectral energy distribution (SED) of the Sgr B2 (N), (M) and (S) cores, and the extended envelope, using the imaging to set the angular size of the components, to derive parameters such as dust temperature.

The integrated line emission $\int T_B dv$ plotted in Figs. 3 to 6 is related the the column density of the molecule in the upper state of the transition N_u by
$N_u = (8\pi\nu^2 k/hc^3 A_{ul}) \int T_B dv$
where A_{ul} is the Einstein coefficient, and assuming optically thin emission (optical depth $\tau \ll 1$). This is related to the total column density of the molecule N, assuming local thermodynamic equilibrium (LTE) by
$N = N_u(Q_T/g_u)\exp(E_u/kT_{ex})$
where g_u is the statistical weight of the upper level, Q_T is the partition function at excitation temperature T_{ex} and E_u is the energy of the upper level. In this simple case, then, the integrated line emission $\int T_B dv$ traces the molecule column density N, and we can use this to trace chemical variations in the Sgr B2 complex. However, the simplifying assumptions are often not valid, so the relation is more complicated.

Firstly, some transitions are not in LTE, as shown by the differences between the three methanol (CH_3OH) lines in Fig. 4, which include maser transitions. Secondly, even if the lines are in *local* thermodynamic equilibrium, there are large gradients in the kinetic temperature T_K and radiation environment (corresponding to radiation temperature T_r) giving gradients in excitation temperature T_{ex}. So transitions from higher energy states will preferentially highlight higher temperature regions. Thirdly, the lines are often not optically thin, so that the optically thick emission is not simply proportional to the column density N_u, in the sense that the integrated intensity saturates for high optical depth in regions of high column density. Fourthly, we have, so far, ignored the full radiative transfer model in which background continuum radiation can be absorbed by the molecules in the cloud, as well as the molecules emitting. With a background continuum source of brightness temperature T_C, we obtain

$$\begin{aligned} T_B &= T_{ex}[1 - \exp(-\tau)] + T_C \exp(-\tau) \\ &= T_{ex} + (T_C - T_{ex})\exp(-\tau) \\ &\approx T_C + (T_{ex} - T_C)\tau \text{ for } \tau \ll 1. \end{aligned}$$

Typically, the spectral line data (as in this paper) are base-level subtracted, to be the line only, but the effect of the background continuum is to reduce the line intensity, and for $T_C > T_{ex}$ the line becomes negative in intensity, i.e. is seen in absorption.

Most of the lines presented here are dominated by emission from the extended, cooler ($T_{dust} \sim 20$ K), envelope, rather than the compact hot cores. The scale of this envelope is around 2 arcmin, but elongated north-south in equatorial coordinates (as shown in the mid-IR, Fig. A1). This envelope is centred to the east of the line of hot cores Sgr B2 (N), (M) and (S), with the north cloud to the north of the hot cores. In Galactic coordinates, this corresponds to a ridge, wrapping around the hot cores, as shown in the first principal components of the 7-mm (Fig. 8) and 3-mm lines (Fig. 10). There are also chemical differences, for example with HNCO and $HOCO^+$ preferentially found (Fig. 6) in the north cloud. The effective spatial scale of the stronger, optically thick lines, such as SO, SiO and CS (Fig. 5) is larger, with the emission filling the whole 6×6 arcmin^2 area imaged, as the central peak emission saturates (and there is absorption). The optically thin isotopologues (^{29}SiO, ^{13}CS and $C^{34}S$, Fig. 5) give a better tracer of the extent of the envelope.

The recombination lines (Fig. 1) show the distribution of the 7-mm free-free radio continuum, assuming that there is not a very large spatial variation in the line to continuum ratio (so that the line emission traces the continuum distribution). The deconvolved angular size (from these recombination lines) is 2.2×0.9 arcmin^2, and the fit to the radio flux densities (Fig. A2 and Table A2) shows that around half the flux comes from the extended envelope and half from the compact hot cores. The spatial distribution along the line of sight of the Sgr B2 components is not well constrained, but the spectral energy distribution (SED) fitting (Appendix) does indicate that Sgr B2 (N) is behind at least part of the dust envelope. Many of the 7-mm molecular lines in Figs. 3 to 6 show absorption centred near Sgr B2 (N) and (M) which matches well the position and scale of the 7-mm free-free continuum (as probed by the recombination lines in Fig. 1).

With a flat spectral index ($\alpha = -0.17 \pm 0.07$ for the total free-free) in the optically thin regime, the continuum brightness temperature falls steeply with frequency $T_C \propto \nu^{\alpha-2}$. The conditions for absorption of the continuum radiation, by the intervening cool envelope (T_C significant compared to T_{ex}), are commonly met in these 7-mm data, as highlighted in the second principal component of Fig. 8. Similar absorption occurs for the 3-mm data of Jones et al. (2008a) (seen in the second principal component of Fig. 10). At these higher frequencies, the absorption at the hot cores Sgr B2 (N) and (M) dominates over the absorption due to the extended envelope. The resolution is higher, the cores contribute a larger fraction of the free-free continuum, and have a higher brightness temperature.

In both the 7-mm and 3-mm molecular lines, there are also lines that peak at the Sgr B2 (N) and (M) hot cores, due to their different chemical conditions and higher temperature.

6 SUMMARY

We have undertaken a line imaging survey of the Sgr B2 region from 30 to 50 GHz (the 7-mm band) with the 22-m single-dish Mopra telescope. This complements the Mopra 3-mm line imaging of Sgr B2 presented in Jones et al. (2008a). Integrated emission images of 47 lines are presented: 38 molecular lines and 9 radio recombination lines.

The distribution of individual lines are discussed, and we have studied the similarities and differences between the lines with principal component analysis (PCA). The major features from the PCA are extended emission from the ridge and north cloud to the north and east of the Sgr B2 (N) and (M) hot cores, and absorption near Sgr B2 (N) and (M). These statistical features are interpreted in terms of the physical components of the Sgr B2 complex (discussed in the appendix) of the extended low temperature envelope, and compact hot cores Sgr B2 (N), (M) and (S). The 7-mm free-free emission in the area of Sgr B2 (N) and (M) is absorbed in this line-of-sight by the envelope.

ACKNOWLEDGMENTS

The Mopra telescope is funded by the Commonwealth of Australia as a National Facility managed by CSIRO as part of the Australia Telescope. The UNSW-MOPS Digital Filter Bank used for the observations with the Mopra telescope was provided with support from the Australian Research Council (ARC), together with the University of New South Wales, University of Sydney and Monash University. We also acknowledge ARC support through Discovery Project DP0879202. PAJ acknowledges partial support from Centro de Astrofísica FONDAP 15010003 and the Gemini-CONICYT Fund. We thank John B. Whiteoak for the 1.2-mm SIMBA data.

REFERENCES

Belloche A., Comito C., Hieret C., Menten K. M., Schilke P., Müller H. S. P., 2005, in Lis D.C., Blake G.A., Herst E., eds, Proc. IAU Symp. 231, Astrochemistry: Recent Successes and Current Challenges. Cambridge Univ. Press, Cambridge, p. 332

Belloche A., Comito C., Hieret C., Menten K. M., Müller H. S. P., Schilke P., 2007, in Lemaire J. L., Combes F., eds, Molecules in Space & Laboratory. S. Diana, Paris, p. 10

Caswell J. L., 1996, MNRAS, 283, 606

Chengalur J. N., Kanekar N., 2003, A&A, 403, L43

Chung H. S., Ohishi M., Morimoto M., 1994, JKAS, 27, 1

Crocker R. M., Jones D., Protheroe R. J., Ott J., Ekers R., Melia F., Stanev T., Green A., 2007, ApJ, 666, 934

Cummins S. E., Linke R. A., Thaddeus P., 1986, ApJS, 60, 819

Dahmen G. et al., 1997, A&AS, 126, 197

de Pree C. G., Gaume R. A., Goss W. M., Claussen M. J., 1996, ApJ, 464, 788

de Vicente P., Martin-Pintado J., Wilson T. L., 1997, A&A, 320, 957

Garwood R. W., 2000, in Manset N., Veillet C., Crabtree D., eds, ASP Conf. Ser. Vol. 216, Astronomical Data Analysis Software and Systems IX. Astron. Soc. Pac., San Francisco, p. 243

Gaume R. A., Claussen M. J., 1990, ApJ, 351, 538

Gaume R. A., Claussen M. J., de Pree C. G., Goss W. M., Mehringer D. M., 1995, ApJ, 449, 663

Goldsmith P. F., Snell R. L., Hasegawa T., Ukita N., 1987, ApJ, 314, 525

Gordon M. A., Berkermann U., Mezger P. G., Zylka R., Haslam C. G. T., Kreysa E., Sievers A., Lemke R., 1993, A&A, 280, 208

Hasegawa T., Sato F., Whiteoak J. B., Miyawaki R., 1994, ApJ, 429, L77

Hasegawa T., Arai T., Yamaguchi N., Sato F., 2008, Ap&SS, 313, 91

Heyer M. H., Schloerb F. P., 1997, ApJ, 475, 173

Hollis J. M., Jewell P. R., Remijan A. J., Lovas F. J., 2007, ApJ, 660, L125

Irvine W. M. et al., 1988, ApJ, 334, L107

Jones P. A. et al., 2008a, MNRAS, 386, 117

Jones P. A., Burton M. G., Cunningham M. R., 2008b, in Kramer C., Aalto S., Simon R., eds, Far-Infrared Workshop 2007, EAS Publ. Ser. 31, EDP Sciences, Les Ulis, p. 77

Jones P. A., Burton M. G., Lowe V., 2008c, in Kwok S.,

Sandford S, eds, Organic Matter in Space, Proc. IAU Symp., 251, Cambridge Univ. Press, Cambridge, p. 257
Kuan Y.-J., Snyder L. E., 1994, ApJS, 94, 651
Kuan Y.-J., Mehringer D. M., Snyder L. E., 1996, ApJ, 459, 619
Lang C. C., Palmer P., Goss W. M., 2008, Galactic Cent. Newsletter, 27, 5 (arXiv:0801.2168)
Liechti S., Wilson T. L., 1996, A&A, 314, 615
Lis D. C., Goldsmith P. F., 1991, ApJ, 369, 157
Lo N. et al., 2009, MNRAS, 395, 1021
Lovas F.J., Dragoset R.A., 2004, J. Phys. Chem. Ref. Data 33, 177
Martin-Pintado J., de Vicente P., Fuente A., Planesas P., 1997, ApJ, 482, L45
McGrath E. J., Goss W. M., De Pree C. G., 2004, ApJS, 155, 577
Mehringer D. M., Menten K. M., 1997, ApJ, 474, 346
Mehringer D. M., Goss W. M., Palmer P., 1994, ApJ, 434, 237
Mezger P. G., Zylka R., Wink J. E., 1990, A&A, 228, 95
Minh Y.-C., 2007, J. Kor. Astron. Soc., 40, 61
Minh Y. C., Irvine W. M., 2006, New Astron., 11, 594
Minh Y. C., Irvine W. M., Ziurys L. M., 1988, ApJ, 334, 175
Minh Y. C., Haikala L., Hjalmarson A., Irvine W. M., 1998, ApJ, 498, 261
Nummelin A., Bergman P., Hjalmarson A., Friberg P., Irvine W. M., Millar T. J., Ohishi M., Saito S., 1998, ApJS, 117, 427
Nummelin A., Bergman P., Hjalmarson Å., Friberg P., Irvine W. M., Millar T. J., Ohishi M., Saito S., 2000, ApJS, 128, 213
Ohishi M., Ishikawa S.-I., Amano T., Oka H., Irvine W. M., Dickens J. E., Ziurys L. M., Apponi A. J., 1996, ApJ, 471, L61
Oka T., Hasegawa T., Sato F., Tsuboi M., Miyazaki A., 1998, ApJS, 118, 455
Pei C. C., Liu S.-Y., Snyder L. E., 2000, ApJ, 530, 800
Pierce-Price D. et al., 2000, ApJ, 545, L121
Pickett H. M., Poynter I. R. L., Cohen E. A., Delitsky M. L., Pearson J. C., Muller H. S. P., 1998, J. Quant. Spectrosc. & Rad. Transfer, 60, 883
Protheroe R. J., Ott J., Ekers R. D., Jones D. I., Crocker R. M., 2008, MNRAS, 390, 683
Reid M. J., Menten K. M., Zheng X. W., Brunthaler A., Xu Y., 2009, ApJ, 705, 1548
Remijan A. J., Hollis J. M., Jewell P. R., Lovas F. J., 2008, AAS, 40, 188
Sato F., Hasegawa T., Whiteoak J. B., Miyawaki R., 2000, ApJ, 535, 857
Sault R. J., Teuben P. J., Wright M. C. H., 1995, in Shaw R. A., Payne H. E., eds, Astronomical Data Analysis Software and Systems IV, Astron. Soc. Pac. Conf. Ser. 77, Astron. Soc. Pac., San Francisco, p. 433
Sawada T., Hasegawa T., Handa T., Cohen R. J., 2004, MNRAS, 349, 1167
Tsuboi M., Handa T., Ukita N., 1999, ApJS, 120, 1
Turner B. E., 1989, ApJS, 70, 539
Turner B. E., Friberg P., Irvine W. M., Saito S., Yamamoto S., 1990, ApJ, 355, 546
Ungerechts H., Bergin E. A., Goldsmith P. F., Irvine W. M., Schloerb F. P., Snell R. L., 1997, ApJ, 482, 245
Val'tts I. E., Colomer F., Shanin G., Gomez-Gonzalez J., Bachiller R., 1991, Astronomicheskii Zhurnal, 68, 456
Urquhart, J. S., Hoare, M. G., Purcell, C. R., Brooks, K. J., Voronkov, M. A., Indermuehle, B. T., Burton, M. G., Tothill, N. F. H., Edwards, P. G., 2010, Characterisation of the Mopra Radio Telescope at 16–50 GHz, preprint arXiv:1005.5036.
Wilson T. L., Snyder L. E., Comoretto G., Jewell P. R., Henkel C., 1996, A&A, 314, 909
Wilson T. L., Rohlfs K., Hüttemeister S., 2009, Tools of Radio Astronomy, Springer-Verlag, Berlin
Zapata L. A., Menten K., Reid M., Beuther H., 2009, ApJ, 691, 332

APPENDIX A: THE COMPONENTS OF SGR B2

The Sgr B2 complex is very complicated, with many physical components distinguishable at high resolution, see for example Mehringer & Menten (1997) and Gaume et al. (1995). However, for many observations with resolution of order tens of arcseconds (Fig. A1) it is common, and physically useful, to consider the three dense cores Sgr B2 (N), (M) and (S), and distinguish them from the larger and less dense envelope.

The three dense cores are prominent in both the radio free-free and sub-mm dust continuum, as shown in Fig. A1, and the (M) and (S) cores are prominent in the mid-infrared. The sub-mm dust distribution also shows the extended component, centred slightly to the west of the line of dense cores, with an extension to the north. As we pointed out in Jones et al. (2008a), many of the 3-mm molecular lines follow the ridge of this extended dust component, while other lines are associated with the dense cores. We find similar distributions here for the 7-mm molecular lines, so for more detailed quantitative discussion of these 7-mm and 3-mm line data, we have undertaken an analysis of the Sgr B2 continuum data.

The structure of the Sgr B2 complex has been analysed by Gordon et al. (1993) using the spectral energy distribution (SED) of the total complex and components FIR1, FIR2 and FIR3 in their nomenclature, corresponding to (N), (M) and (S).

The peak in the SED due to dust is modelled as a Black Body modified by the optical depth τ_ν of the dust, so the flux density S_ν divided by the source solid angle Ω is $S_\nu/\Omega = B_\nu(T)(1 - \exp(-\tau_\nu))$ where $B_\nu(T)$ is the Planck function (Wilson, Rohlfs, Hüttemeister 2009). The dust optical depth is assumed to be proportional to the gas column density, with some empirical scaling factor. The model from Mezger, Zylka, & Wink (1990) is used with $\tau_\nu = (N_H/1.4 \times 10^{20}\mathrm{cm}^{-2})(\lambda/\mu\mathrm{m})^{-2} b(Z/Z_\odot)$, where N_H is the total hydrogen column density, $(Z/Z_\odot)$ is the metallicity, assumed 2 for the Galactic Centre and b is a dust parameter, with $b = 3.4$ for hydrogen number density $n_H \geqslant 10^6$ cm^{-2} and $b = 1.9$ for $n_H \leqslant 10^6$ cm^{-2}.

The observed flux densities in the dust SED can be fitted with 3 parameters; temperature T, solid angle Ω and the wavelength $\lambda_{\tau=1}$ at which the optical depth is unity, related by the above equation to the column density N_H. (In this model the power-law index of the dust optical depth

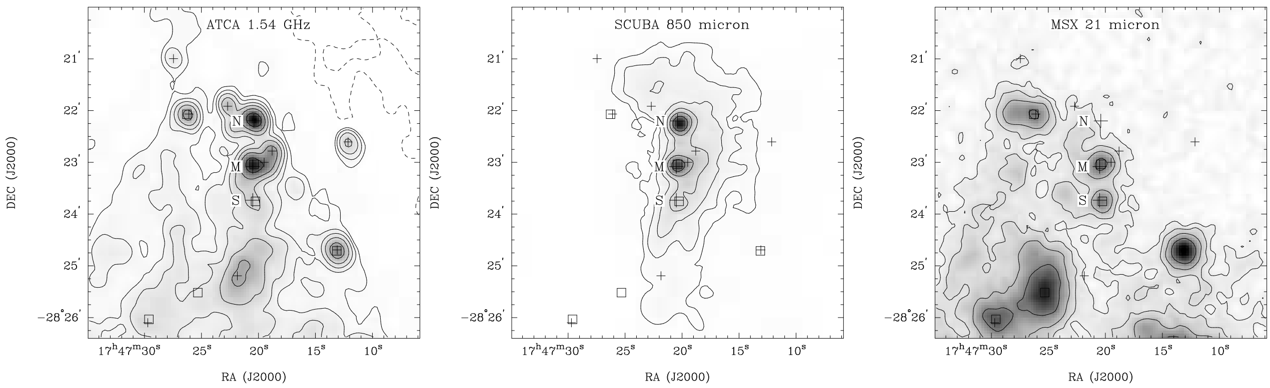

Figure A1. The continuum images of the Sgr B2 complex in radio (ATCA 1.54 GHz), sub-mm (SCUBA 850 μm) and mid-infrared (MSX 21 μm), showing the Sgr B2 (N), (M) and (N) cores. The radio and mid-infrared trace star formation, with some extra compact features, and extended emission to the south-east. The sub-mm traces warm and cold dust, including diffuse emission around the cores. Note that these images are in equatorial coordinates, rather than Galactic coordinates used in the main body of this paper, but the crosses for radio peaks and open squares for infrared peaks are used as fiducial marks.

is $\beta = 2$: other models can have different power law slopes β, but we leave β fixed here to reduce the number of free parameters in the fit.)

We plot in Fig. A2 the SED of the Sgr B2 components, using the data from Gordon et al. (1993) plus some additional data, from more recent observations.

We include fluxes from Kuan, Mehringer, & Snyder (1996) for the compact components in the 3-cm and 3-mm bands (combining their N and N′ into the one source).

We have fitted data from our own observations with the ATCA at 1.54 GHz (Fig. A1) and 36 GHz (Fig. 2) and with SIMBA on SEST at 1.2 mm. The fitting was done with multiple gaussians using the task *imfit* in the MIRIAD package, to obtain angular size information as well as flux densities.

We have also fitted data obtained as FITS images from several public databases. In the radio we obtained VLA images at 20 cm, 3.6 cm, 9 GHz (3.3 cm) and BIMA data at 3 mm from the Astronomy Digital Image Library (ADIL)[10]. In the sub-mm we obtained JCMT SCUBA[11] images at 450 and 850 μm and recent CSO BOLOCAM[12] images at 1.1 mm. In the mid-infrared we obtained MSX[13] images at 8, 12, 15 and 21 μm, and IRAS reprocessed HIRES[14] images at 60 and 100 μm.

The extra flux density data are summarised in Table A1.

The flux density data (Fig. A2) show two physical components, the dust peak around 1.5 THz (200 μm) and the optically thin free-free emission between 3 and 100 GHz. There are, however, problems in using flux densities obtained from data obtained with a range of spatial resolutions. For the fitting of the complex structure with the components Sgr B2 (N), (M) and (N), and total flux, different amounts of flux will be included depending on the size of the telescope beam (as the four components are a simplification). This leads to discrepancies in the flux densities, even considering the quoted uncertainties. We have fitted models to the SEDs, despite this, but note that the reduced χ^2 of the fits are high.

Table A1. Fitted flux densities used for the Sgr B2 spectral energy distribution, in addition to values from the literature.

Frequency or Wavelength	Telescope Project or Instrument	Total Jy	Flux density N Jy	M Jy	S Jy
1.54 GHz	ATCA		2.35	2.57	0.13
9.1 GHz	VLA		6.3	7.9	0.64
36 GHz	ATCA		6.1	8.0	
1.2 mm	SIMBA	330	103	71	3.7
1.1 mm	BOLOCAM	420	64	90	25
0.85 mm	SCUBA	2500	330	260	22
0.45 mm	SCUBA	68000	3200	3300	720
100 μm	IRAS	65000			
60 μm	IRAS	14500			
21 μm	MSX			16.4	9.5
15 μm	MSX			1.80	2.13
12 μm	MSX			1.07	0.96
8 μm	MSX			0.79	0.83

For the free-free component, we have fitted power laws over the frequency range up to around 100 GHz, excluding some points for Sgr B2 (N) and the total which show some upturn due to the dust component. For the dust component we fitted the 3-parameter model discussed above. For Sgr B2 (N), as we discuss below, we also follow Gordon et al. (1993) in including an extra absorption term for dust along the line of sight, making a 4-parameter fit $S_\nu = \Omega B_\nu(T)(1 - \exp(-\tau_{\nu,1})) \exp(-\tau_{\nu,2})$. The dust fit used the data around 100 GHz for Sgr B2 (N) and the total, after correction for the free-free component. The fitting was done in the GNUPLOT package, which uses the nonlinear least-squares (NLLS) Marquardt-Levenberg algorithm. For the total flux, we fitted the data after subtracting the models for the compact components Sgr B2 (N), (M) and (S), so that

[10] http://imagelib.ncsa.uiuc.edu/imagelib.html. Note that some of the archived radio images from ADIL were not suitable for measuring flux densities, as the images were not primary beam corrected, but they were useful for measuring sizes of the compact components.
[11] http://www3.cadc-ccda.hia-iha.nrc-cnrc.gc.ca/jcmt/
[12] http://irsa.ipac.caltech.edu/data/BOLOCAM_GPS/
[13] http://irsa.ipac.caltech.edu/applications/MSX/MSX/
[14] http://irsa.ipac.caltech.edu/IRASdocs/hires_over.html

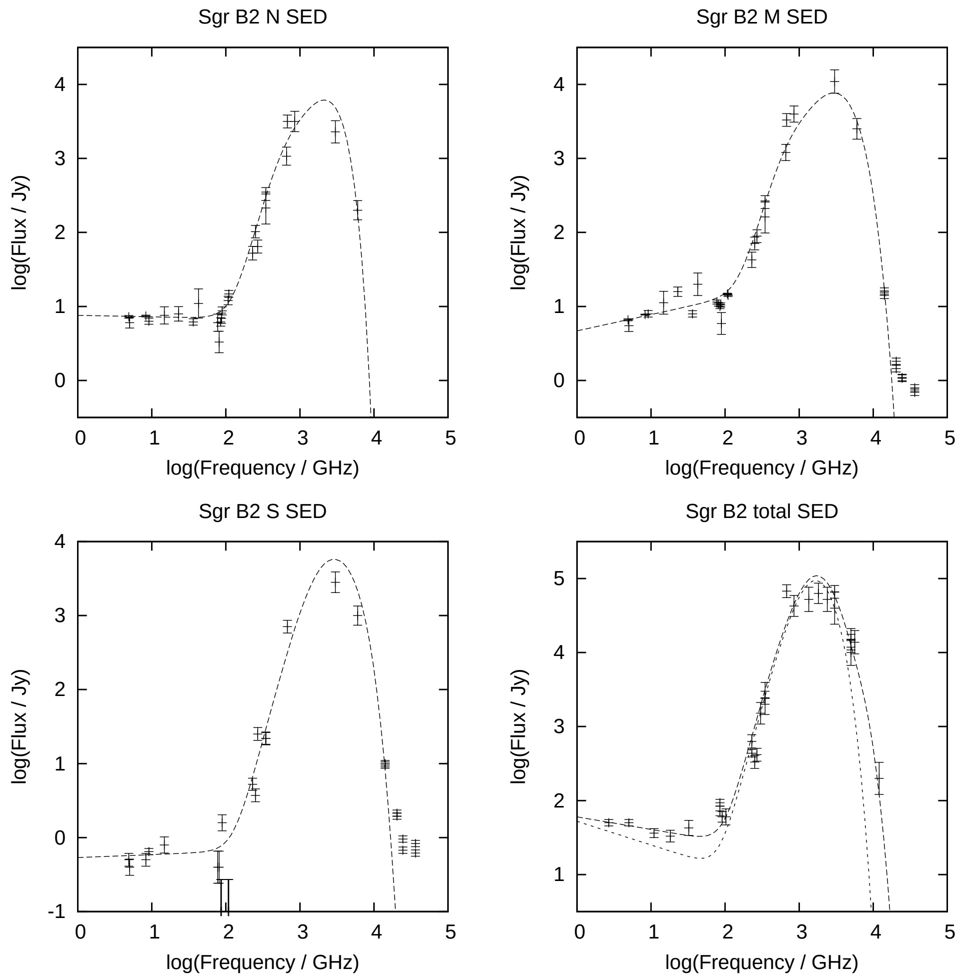

Figure A2. The spectral energy distribution (SED) of the Sgr B2 components (N), (M), (S) and total, from the radio to the infrared, following Gordon et al. (1993), with some additional data. The dashed lines are our schematic fits to the SED, but we note that there are problems using fluxes from the literature with a wide range of spatial resolutions so that the χ^2 value of the model fits are poor. The plot for the total flux has a long dashed line for the total flux points, and a shorter dashed line for the extended envelope which contains most of the flux.

we were actually fitting the model to the extended envelope. The model fits for both the total flux and the extended envelope are both plotted in Fig. A2, and we note that for most of the frequency range, the extended component dominates the total flux.

For the free-free component, we find spectral indices -0.02 ± 0.03, 0.22 ± 0.02, 0.04 ± 0.16 and -0.32 ± 0.12 for the components Sgr B2 (N), (M), (S) and the extended envelope respectively, and flux densities at 30 GHz 7.1 Jy, 9.9 Jy, 0.62 Jy and 17.7 Jy respectively. Note that this indicates that around half the flux is in the extended component which may be missed by the interferometric observations (e.g. Fig 2). We do attribute the radio emission from 3 to 100 GHz in the compact components to optically thin free-free emission, with basically a flat spectrum, although the rising spectrum of Sgr B2 (M) may indicate some of the subcomponents are ultracompact H II regions with the turnover from optically thick to optically thin above 10 GHz. The spectrum of the total Sgr B2 flux is flat (spectral index -0.17 ± 0.07), but when we subtract the compact components, notably Sgr B2 (M) with the rising spectrum, the residual extended component has a somewhat steeper spectrum.

There has been some discussion of non-thermal radio emission from Sgr B2 by Hollis et al. (2007), Crocker et al. (2007) and Protheroe et al. (2008). We agree with Lang, Palmer, & Goss (2008) and Protheroe et al. (2008) that due to the complex structure of Sgr B2, it is difficult to measure the radio spectral index accurately by combining observations with different resolutions which may be including different features. In particular, the fluxes measured with the GBT by Hollis et al. (2007) for Sgr B2 (N) will include flux from the extended component, to a greater extent at the lower frequencies with the larger beam.

The fits to the dust components, for free parameters T, Ω and $\lambda_{\tau=1}$ gave similar results to that of Gordon et al. (1993), as expected since the data used here is based on their compilation. However, there are quite large uncertainties in derived Ω and $\lambda_{\tau=1}$, and the two parameters are highly correlated. We decided, therefore, to constrain the fits by using a fixed derived value for the dust solid angle Ω obtained using the extra spatial information from the sub-mm images.

Table A2. Parameters for the Sgr B2 components fitted from the SED, and derived from these fits. From the fit to the optically-thin free-free part of the spectrum, we obtain the spectral index α_{ff} and the flux density S_{30} at reference frequency 30 GHz. We choose to fix the angular size of the dust component to that measured from the sub-millimetre images, and derive the dust temperature T_d and turnover wavelength $\lambda_{\tau=1}$ from the dust peak in the spectrum. The total hydrogen column density N_H, number density n_H and mass M_H are derived from the dust spectrum fits, as described in the text.

Component	α_{ff}	S_{30} Jy	Ω fixed arcsec^2	Spatial scale pc	T_d K	$\lambda_{\tau=1}$ μm	N_H 10^{24} cm^{-2} (10^{28} m^{-2})	n_H 10^6 cm^{-3} (10^{12} m^{-3})	M_H M$_\odot$
N	-0.02 ± 0.03	7.1	117	0.40	65 ± 17	740 ± 150	12	8.9	8600
M	0.22 ± 0.02	9.9	138	0.43	50 ± 1	680 ± 70	9.6	6.8	8400
S	0.04 ± 0.16	0.62	118	0.40	48 ± 1	230 ± 30	1.1	0.87	850
envelope	-0.32 ± 0.12	17.7	17400	4.5	24 ± 2	280 ± 40	3.0	0.19	320000

We used the geometric mean of the deconvolved sizes from the SCUBA 450- and 850-μm images (resolution 7.5 and 14 arcsec), and the 1.3-mm IRAM 30-m image (resolution 11 arcsec), giving gaussian half-widths 10.2, 11.2 and 10.2 arcsec for Sgr B2 (N), (M) and (S). [15] We therefore used solid angles $\Omega = 1.133\theta^2$ of 117, 138 and 118 arcsec^2 for Sgr B2 (N), (M) and (S). For the extended component, we used the geometric mean of effective fitted solid angles from the SCUBA 450- and 850-μm, BOLOCAM 1.1-mm and 1.3-mm IRAM-30-m images, which is $\Omega = 17400$ arcsec^2. [16]

The results from the dust spectrum fits, with Ω fixed, and two free parameters T, and $\lambda_{\tau=1}$ are given in Table A2.

For Sgr B2 (N) we find, as pointed out by Gordon et al. (1993), that the extra line-of-sight absorption component to the model is needed, making in this case then a three parameter fit. In particular, due to the inter-relationship of parameters T, Ω and $\lambda_{\tau=1}$ it is possible to fit the cutoff in the dust SED at high frequencies (infra-red, where Sgr B2 (N) is not detected, see Fig. A1) with a low temperature (T around 30 K) but this requires a large angular size $\Omega \sim 500$ arcsec^2 which is in disagreement with the measured angular size. If we fix the angular size Ω at that measured, then the extra absorption component to the model is clearly required, with the turnover wavelength fitted as $\lambda_{\tau=1} = 100 \pm 17\mu$m, in good agreement with Gordon et al. (1993). This is physically interpreted as Sgr B2 (N) being partly embedded in the envelope.

We also list in Table A2 the parameters derived from the dust spectrum fits of total hydrogen column density N_H, number density n_H and mass M_H for the four components Sgr B2 (N), (M), (S) and envelope. The turnover wavelength $\lambda_{\tau=1}$ is related to total hydrogen column density N_H by $N_H = 1.4 \times 10^{20}\mathrm{cm}^{-2}(\lambda_{\tau=1}/\mu\mathrm{m})^2(\mathrm{Z}_\odot/\mathrm{Z})/\mathrm{b}$ where $Z/Z_\odot$ is the metallicity, assumed 2 for the Galactic Centre, and b is a dust parameter, assumed 3.4 for components Sgr B2 (N), (M) and (S), with $n_H \geqslant 10^{-6}\mathrm{cm}^{-6}$ and 1.9 for the envelope with $n_H \leqslant 10^{-6}\mathrm{cm}^{-6}$ (Gordon et al. 1993; Mezger et al. 1990). The number density n_H and mass M_H are derived using the angular size Ω to estimate the line-of-sight thickness, and hence volume of the components. These are rough estimates, similar to those derived by Gordon et al. (1993) from similar fits, but we assume Galactic Centre distance 8.0 kpc.

We note that the three hot cores Sgr B2 (N), (M) and (S) have similar angular size and temperature, but that Sgr B2 (S) has around an order of magnitude smaller flux density (both dust and free-free components), column density, number density and mass. The extended envelope is cooler but around an order of magnitude larger in diameter than the cores, or two orders of magnitude in solid angle, and dominates the flux density of both dust and free-free components. The envelope is of much lower number density than the cores, but with much greater mass.

We use these parameters of the Sgr B2 components in Section 5 to interpret the molecular line observations of Section 3.

[15] We did not include deconvolved sizes from the BOLOCAM 1.1-mm or SIMBA 1.2-mm images, as the images were lower resolution (33 and 24 arcsec) and hence the deconvolved sizes were much less accurate.
[16] The SIMBA 1.2-mm image may suffer from spatial filtering in the data reduction, affecting the extended structure.

This paper has been typeset from a TEX/ LATEX file prepared by the author.